



CARMA Memorandum Series #63

CARMA Summer School 2014

Melvyn Wright, Marc Pound, Dick Plambeck, John Carpenter, Doug Friedel, Nikolaus Volgenau, Patrick Kelly, Lauranne Lanz, Lauren McKeown, Jay Franck, Erin Cox, Maryam Tabeshian, Andrew Nadolski, Dana Anderson, Scott Barenfeld, Devin Crichton, Ko-Yun Huang, Jonathan Florez, Amy Steele, Ned Molter, Joey Rodriguez, Bandon Decker, Shравan Avadhuta

October 10, 2014

ABSTRACT

The 8th CARMA Summer School was held at the observatory at Cedar Flat 2014 on Aug 3-Aug 9, 2014 with 18 students from Berkeley, Caltech, Illinois, Maryland, Johns Hopkins, Vanderbilt, Fisk, Wesleyan, Trinity College Dublin, Missouri, Cal State, Macalaster, Western Ontario, and Case Western Reserve. A new wrinkle this year is that youtube channel of the lectures was set up for three international students who were unable to attend. The channel was quite successful until Google shut it down, claiming violation of community guidelines. Poor weather hampered observations during the first couple days, but there was still enough good weather during the rest of the week for students to get plenty of data.

During the school, students formed small teams and designed and obtained their own observations, in consultation with the instructors. Using both science subarrays students observed star-forming regions, YSOs and outflows, Saturn, stellar atmospheres, nearby galaxies, a high-z galaxy, and galaxy clusters. At the end of the week, the students gave short presentations on their results. In this memo we collect together some of the results from the student projects.

1. Introduction

The 8th CARMA Summer School was held at the observatory at Cedar Flat on Aug 3-Aug 9, 2014 with 18 students and 6 instructors. As in previous years, the school had the use of the telescope for the week. The array was in the most compact E-configuration. During the school the students had their own observing projects which they worked on during the week as well as attending lectures and demonstrations. Each of the student projects had 5-6 hours of telescope time and the students controlled the telescope for their own projects. The students took the observations, reduced and analyzed the data, and presented the results.

On the first day the students learned how to select suitable observing projects for the CARMA telescope. The introductory lectures covered the characteristics of the telescope, instrumentation, and observing techniques which taught the students to:

- select suitable astronomical sources for observing.
- select the observing frequency, spectral lines to be observed.
- evaluate angular resolution, velocity resolution and sensitivity needed.
- select the correlator setup and calibrations needed.
- prepare an observing script to define the observing procedure at the telescope.
- make the observations

During the rest of the week, the lectures and demonstrations covered the theory and techniques used for millimeter wavelength aperture synthesis and for the CARMA array, and more detailed lectures on the hardware and software, and reducing and analyzing data. As they worked on their projects the students learned how to:

- schedule the telescope effectively.
- calibrate the data.
- make images.
- identify and fix problems that set off the alarm.
- analyze and present the results.

On Friday the students made 10-15 minute presentations and we discussed the results. In all, a very satisfying week seeing all the enthusiasm and so many exciting projects from initial planning and observations, to analysis and results.

2. The CARMA Telescope

The CARMA telescope is an aperture synthesis array, typically operating as two independent subarrays of 15 and 8 antennas, respectively. In the CARMA-15 subarray, there are two receiver bands, 3 mm and 1 mm, and the spectral line correlator. A basic aperture synthesis observation makes an image the size of the primary beam ($\lambda/D \sim 1'$ at 100 GHz; $0.5'$ at 230 GHz) with a resolution corresponding to the maximum separations of the antennas. During the Summer School, CARMA-15 was in the E configuration, with an angular resolution $\sim 10''$ at 100 GHz, and $\sim 5''$ at 230 GHz. The CARMA-8 subarray of eight 3.5m antennas was in the SL configuration for continuum-only projects at 30 GHz (primary beam $\sim 11'$; resolution $\sim 2'$) and 90 GHz (primary beam $\sim 3.6'$; resolution $\sim 40''$). The CARMA-8 correlator produces 7 GHz of continuum data. All antennas can be combined into a single 23-element array, CARMA-23, with 4 GHz of correlator bandwidth.

It's best to observe a strong enough source that one can make an image during the school, rather than a detection project, then the effects of different imaging techniques can be explored. The most convenient source size is one which is smaller than the size of the primary beam when only one pointing is needed. Larger sources can be imaged by time-sharing the pointing of the antennas (mosaicing), at the cost of lowered sensitivity.

The sensitivity is determined by the system noise (receivers plus atmosphere), the bandwidth (or velocity resolution), and the observing time. The atmosphere is usually not so good for 1 mm observations in the summer (although a couple 1 mm projects were run this year), for sources which are at low declinations that must be observed through more of the atmosphere, so select a bright source which is high in the sky and can be observed at 3 mm or 1 cm is preferred. Not all the projects that the students wanted to do satisfied these conditions, so a final list of projects from those proposed was selected on the first day of the school. Students grouped themselves into small teams to work on the selected projects.

2.1. Logistics

Because this is a hands-on school, all lectures and demonstrations were held in the control building and at the telescopes at Cedar Flat. Mel, Marc, Dick, Doug, and 16 of the students stayed in the "Noren" group campground, about 1.5 miles from the control room, and near the antenna pads for the A-configuration. Those who camped avoided the hassle of driving up and down the mountain each day and had a wonderful opportunity to fall asleep under a star-filled and moonless sky each night. The other students stayed in the dorm and cottage at OVRO. Delicious breakfasts, lunches, and dinners were provided at the observatory, prepared by Sarah Landry and Barbara Marzano. Mary Daniel adroitly handled all the accommodations, making sure every one had a place to rest their weary heads at the end of the long days. We organized a hike to Second Lake on Saturday.

3. Mapping the Structure of the L1157-mm Stellar Outflow Shravan Avadhuta (CSU-LA) & Scott Barenfeld (Caltech)

3.1. Introduction

Protostars are surrounded by an envelope of gas and dust accreting onto the still-forming star. Not all of this material makes it onto the star, however. A significant fraction is expelled from the poles of the star, forming a large, bipolar outflow. A classic example of such a system is the well-studied L1157-mm (e.g. Stephens et al. (2013)). Millimeter wavelength observations are sensitive to the thermal emission of the dust in these systems, as well as the CO rotational transitions. As such, we use the CARMA interferometer to study the structure of L1157-mm at a wavelength of 3 mm.

3.2. Observations and Data Reduction

Observations of L1157-mm were carried out using the 15 10.4 m and 6.1 m antennas of the CARMA array in E configuration. The correlator was divided into three 31 MHz windows, centered on the ^{12}CO , ^{13}CO , and C^{18}O (1-0) transitions, and five 500 MHz continuum windows. Observations started on August 11th 2014 at 11:30 pm and continued until August 12th 3:30 am, PST. The weather during the observation was not very favorable with average τ of 1.573 and Phase RMS of $327 \mu\text{m}$. 3C84 was used as a bandpass calibrator, Uranus as a flux calibrator, and 1927+739 as a gain calibrator. Despite the weather conditions, the track proceeded without any alarms. The data required very little flagging except for a few outlying amplitudes for our calibrators. The data were calibrated and maps were generated using the automated scripts provided by John Carpenter.

3.3. Results and Discussion

3.3.1. Dust Continuum

The integrated map generated from our continuum windows is shown in Figure 1. This continuum emission traces the location of dust within the system, which appears to be centrally located within the central $10''$ of the young star. Fitting an elliptical Gaussian to the emission in this region, we find an integrated flux density of 81.6 mJy.

3.3.2. ^{12}CO

Our 31 MHz spectral window centered on 115.271 GHz is sensitive to the ^{12}CO (1-0) transition. Our map of this window shows the bipolar outflow structure of L1157-mm (Figure 2). To investigate the structure of this outflow in velocity space, we integrated 1.25 km/s sections of the ^{12}CO window for

all channels showing ^{12}CO emission upon visual inspection. We see emission for velocities between 13.8 km/s below and 6.6 km/s above 115.271 GHz. Note that L1157-mm is moving away from the Sun with a velocity of several km/s, so it is not unexpected that the above velocity range is not symmetric about 115.271 GHz. Stepping through velocity space, Figure 3 shows that the upper lobe in the outflow is moving with positive velocity (redshifted) with respect to the the central protostar, while the lower lobe is moving with negative velocity (blueshifted). Figure 4 shows the integrated fluxes of all channels showing the upper lobe and all channels showing the lower lobe, respectively. The velocity structure of the outflux indicates it is inclined relative to the line of sight, with the upper lobe tilted away from Earth and the lower lobe towards Earth.

3.3.3. ^{13}CO and C^{18}O

^{13}CO and C^{18}O do not show the same large outflow lobes as ^{12}CO . Figures 5 and 6 show contours of ^{13}CO and C^{18}O , respectively, overlaid on the continuum data. While C^{18}O does not show any emission beyond the central continuum region, ^{13}CO does show a small lobe coming from the central region. Figure 7 shows that this lobe is colocated with the base of the ^{12}CO lobe, as we would expect. It is likely all three CO isotopes are present throughout the outflow, but beyond the small ^{13}CO lobe at the base of the outflow, we only detect ^{12}CO .

3.3.4. Structure of L1157-mm

Figure 8 shows a combined map of our continuum and ^{12}CO data. We see that the continuum dust emission is confined to central dense region around the protostar, while the ^{12}CO emission extends into the outflow lobes $100''$ from the protostar to the edges of our field of view.

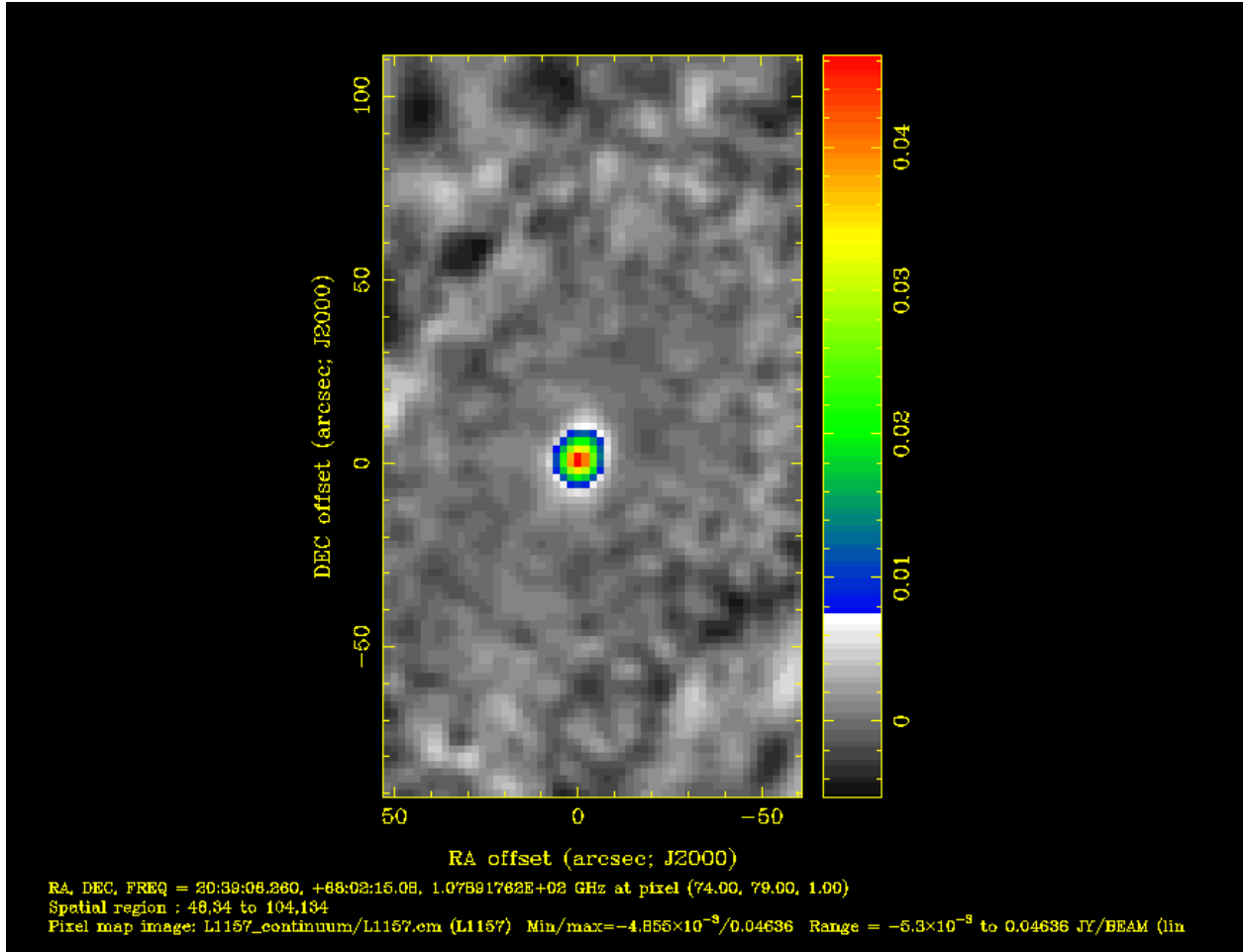


Fig. 1.— Continuum emission at 3mm of L1157-mm, corresponding to dust. The dust is concentrated in the central region around the protostar, and does not appear in the outflow.

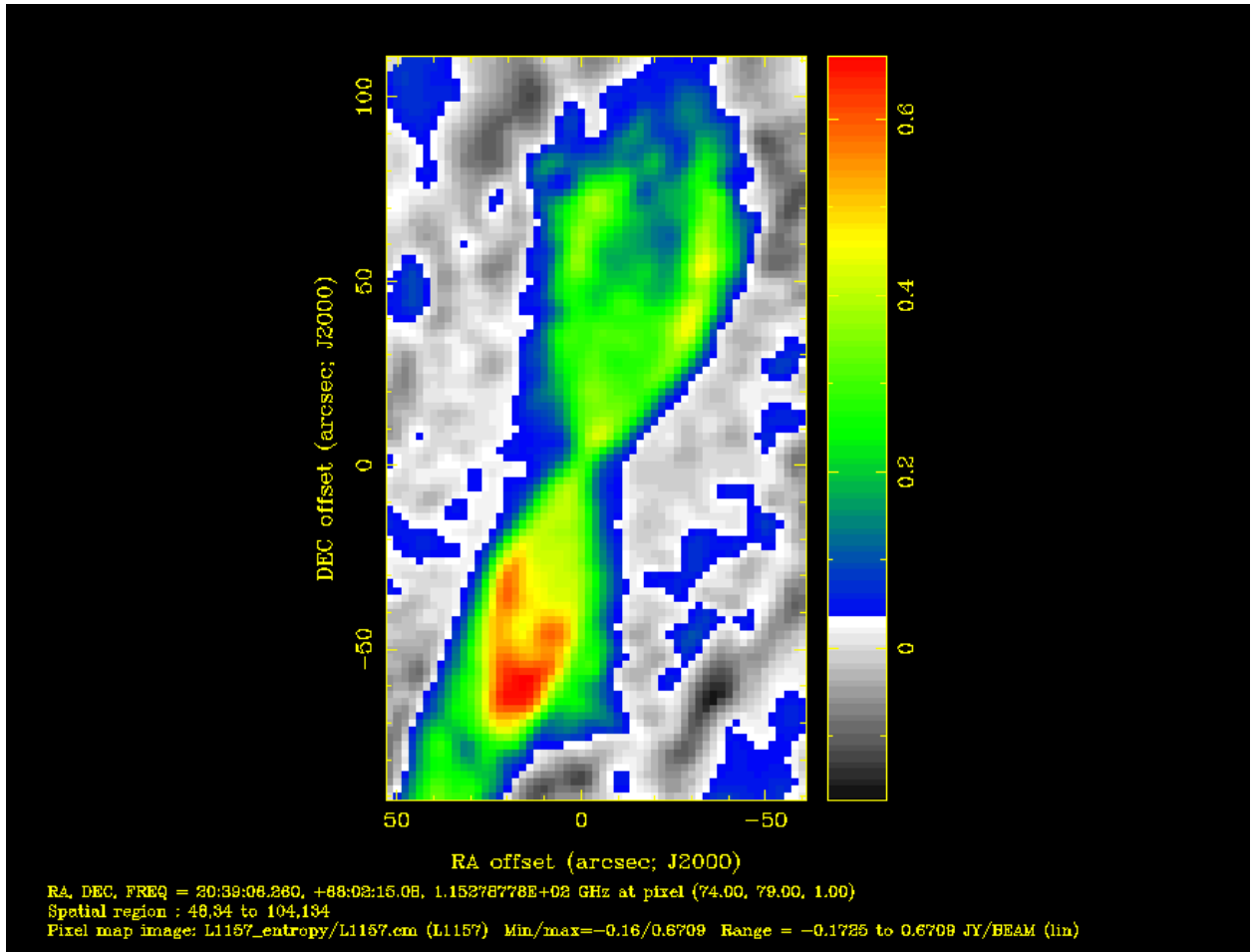


Fig. 2.— ^{12}CO (1-0) emission. The CO traces the outflow from the protostar.

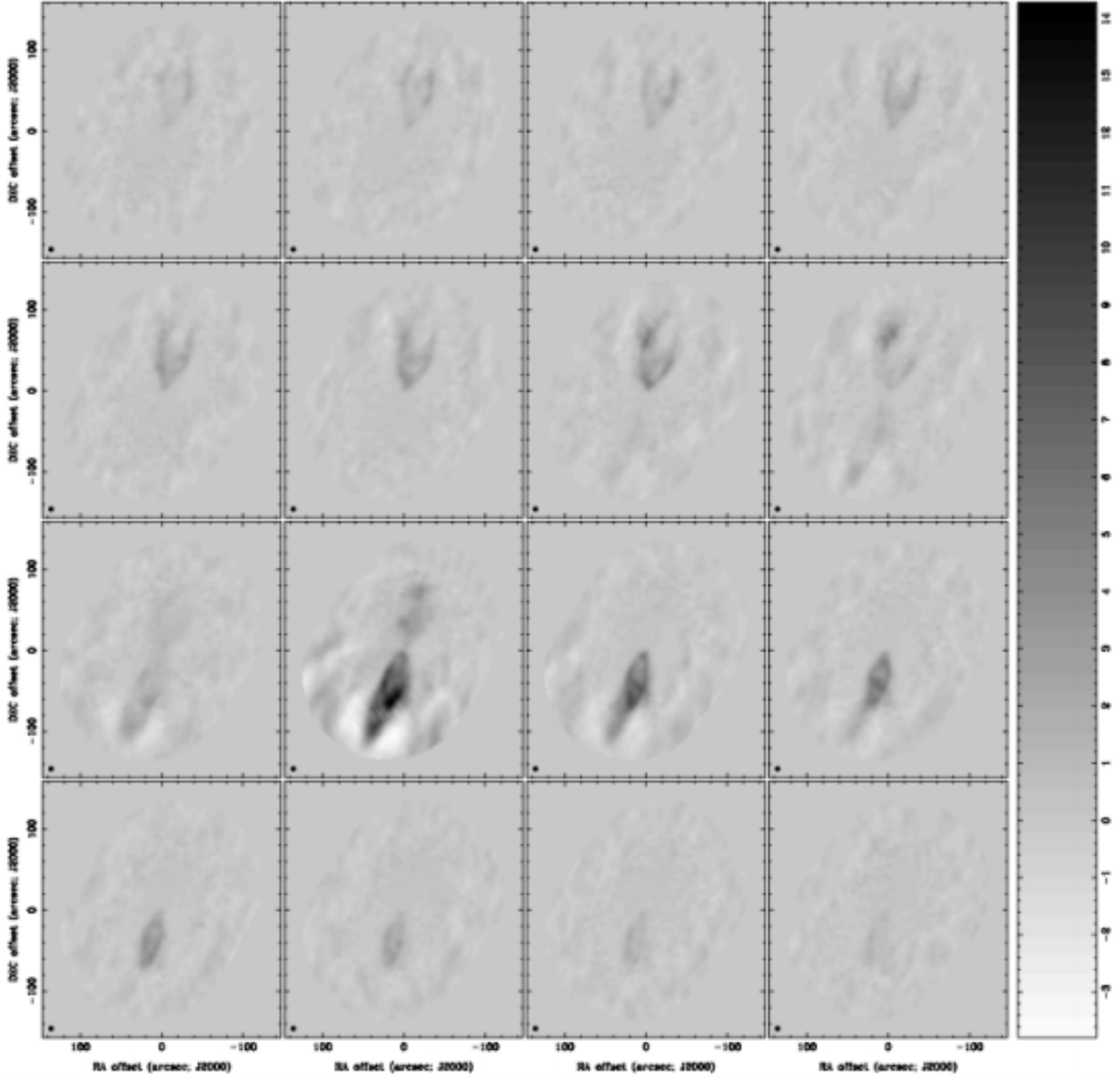


Fig. 3.— ^{12}CO (1-0) emission maps integrated over every 1.25 km/s. The positive (redshifted) velocities show emission in the upper lobe, while the negative (blueshifted) velocities show emission in the lower lobe. This indicates the outflow is inclined with respect to Earth, with the upper lobe tilted away.

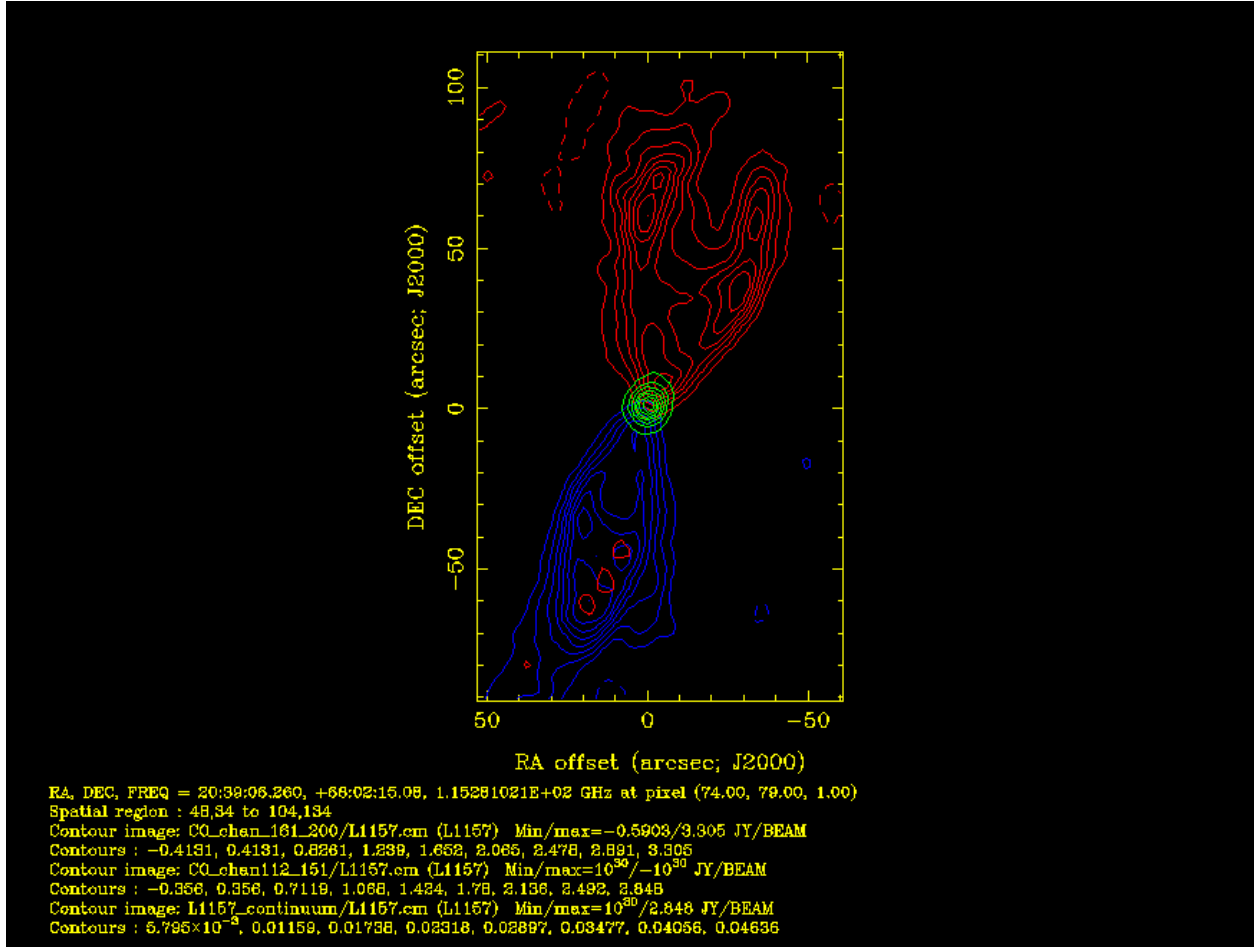


Fig. 4.— ^{12}CO (1-0) contours for the integrated positive velocities (red) and negative velocities (blue). Dust continuum emission is shown in green.

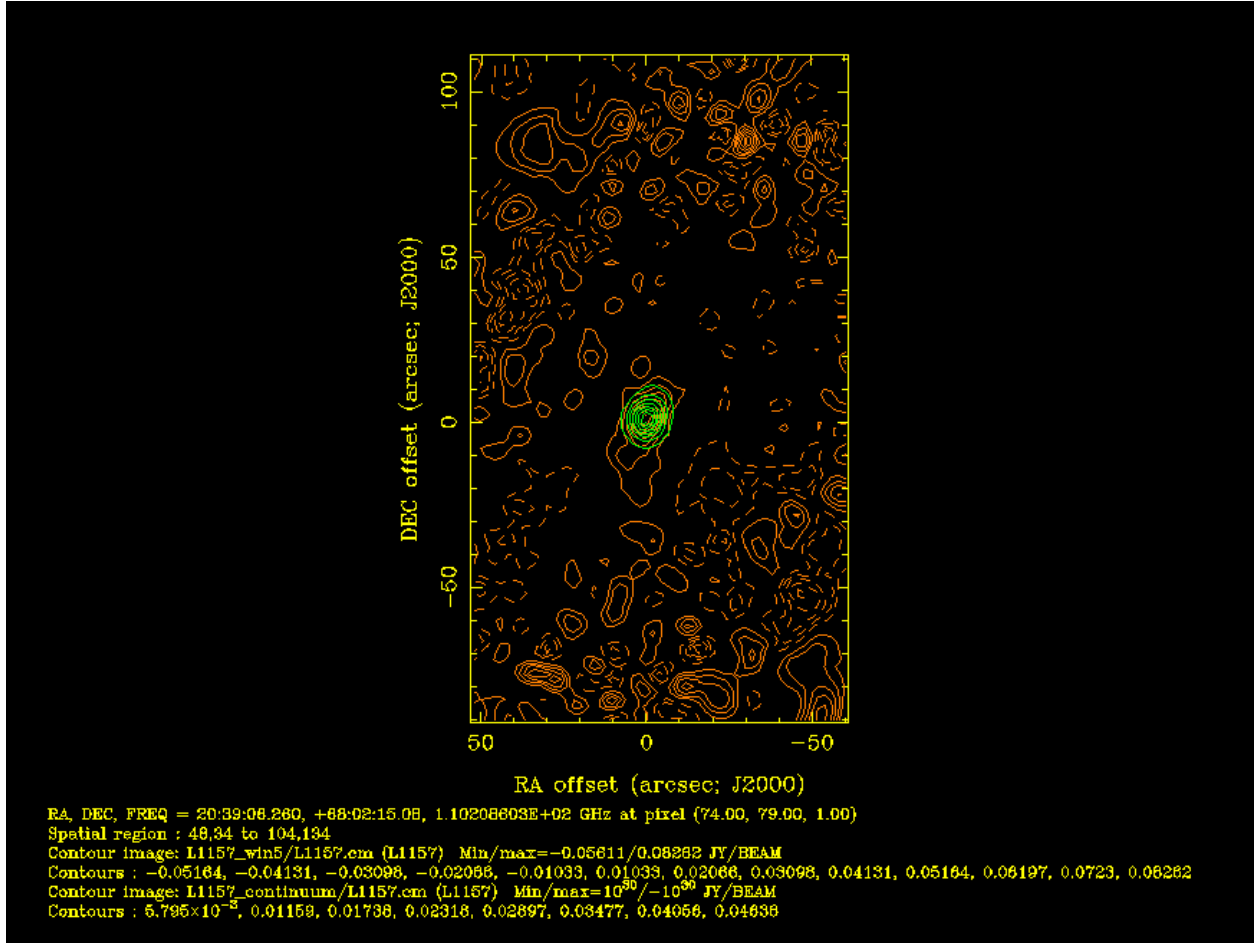


Fig. 5.— ¹³CO (1-0) contours (red) overlaid on the continuum emission (green). ¹³CO is visible in the central envelope, as well as in the base of the lower part of the outflow.

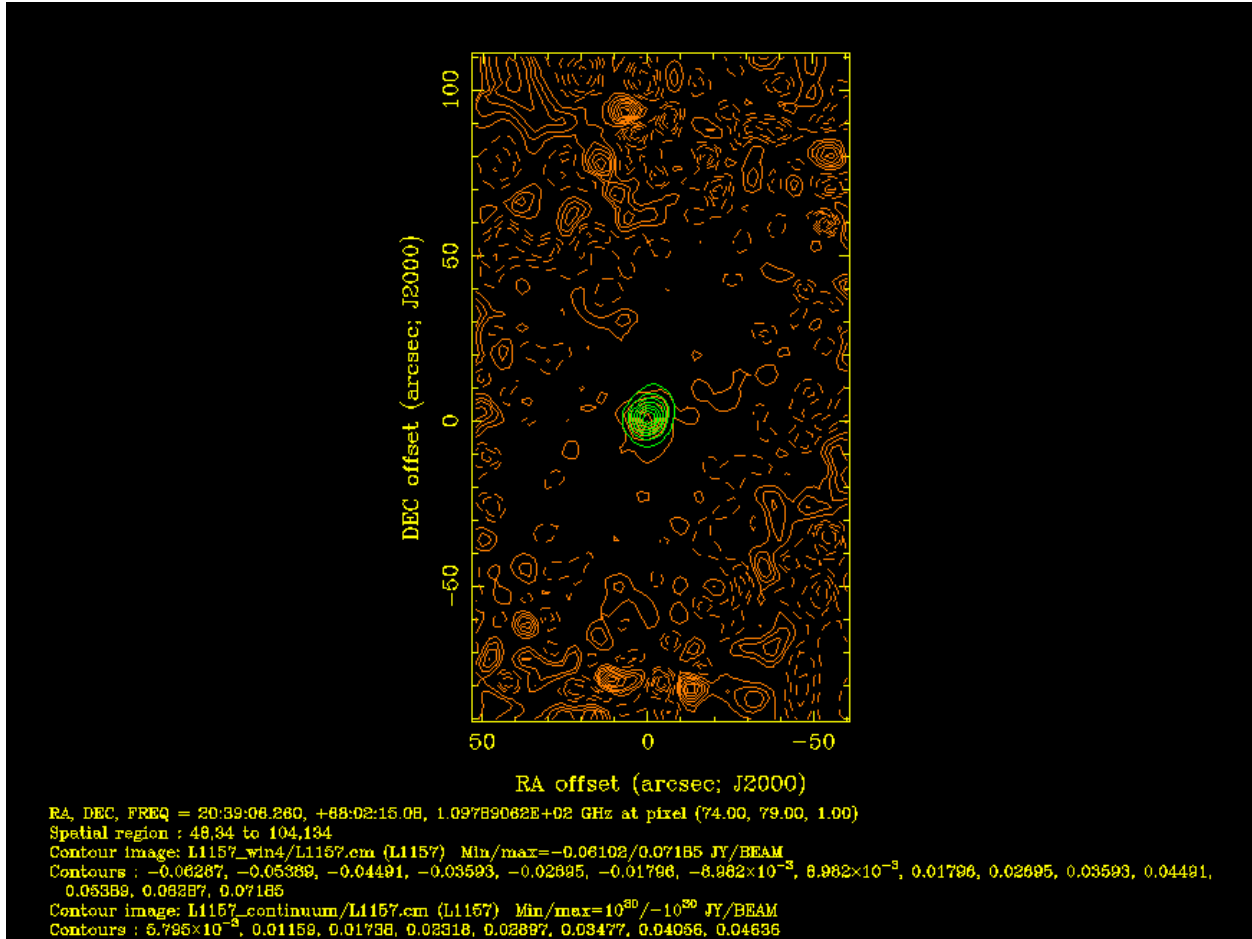


Fig. 6.— C¹⁸O (1-0) contours (red) overlaid on the continuum emission (green). No C¹⁸O is visible outside of the central envelope.

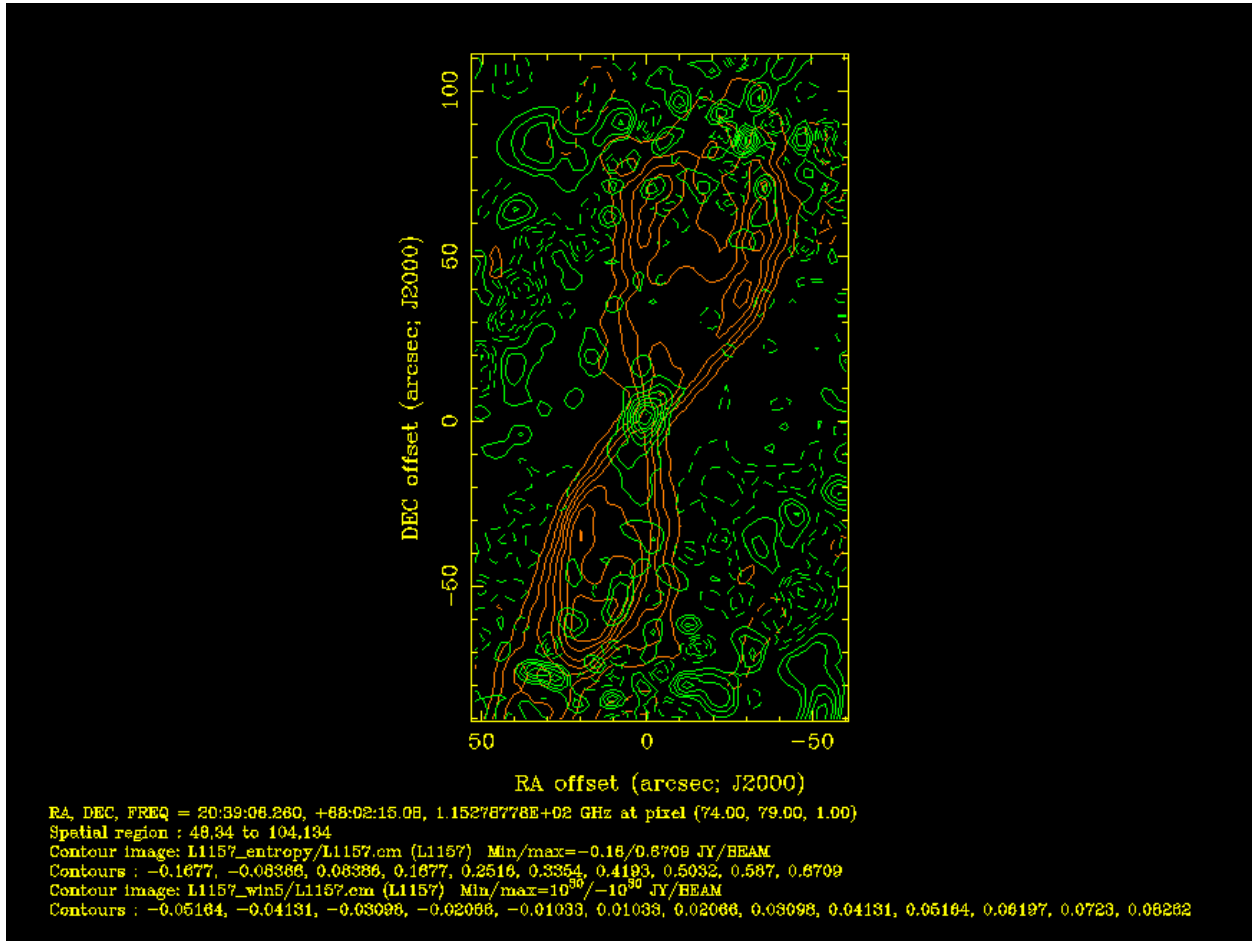


Fig. 7.— ^{13}CO (1-0) contours (green) overlaid on the ^{12}CO (1-0). The outflow structure of ^{13}CO traces the lower ^{12}CO outflow.

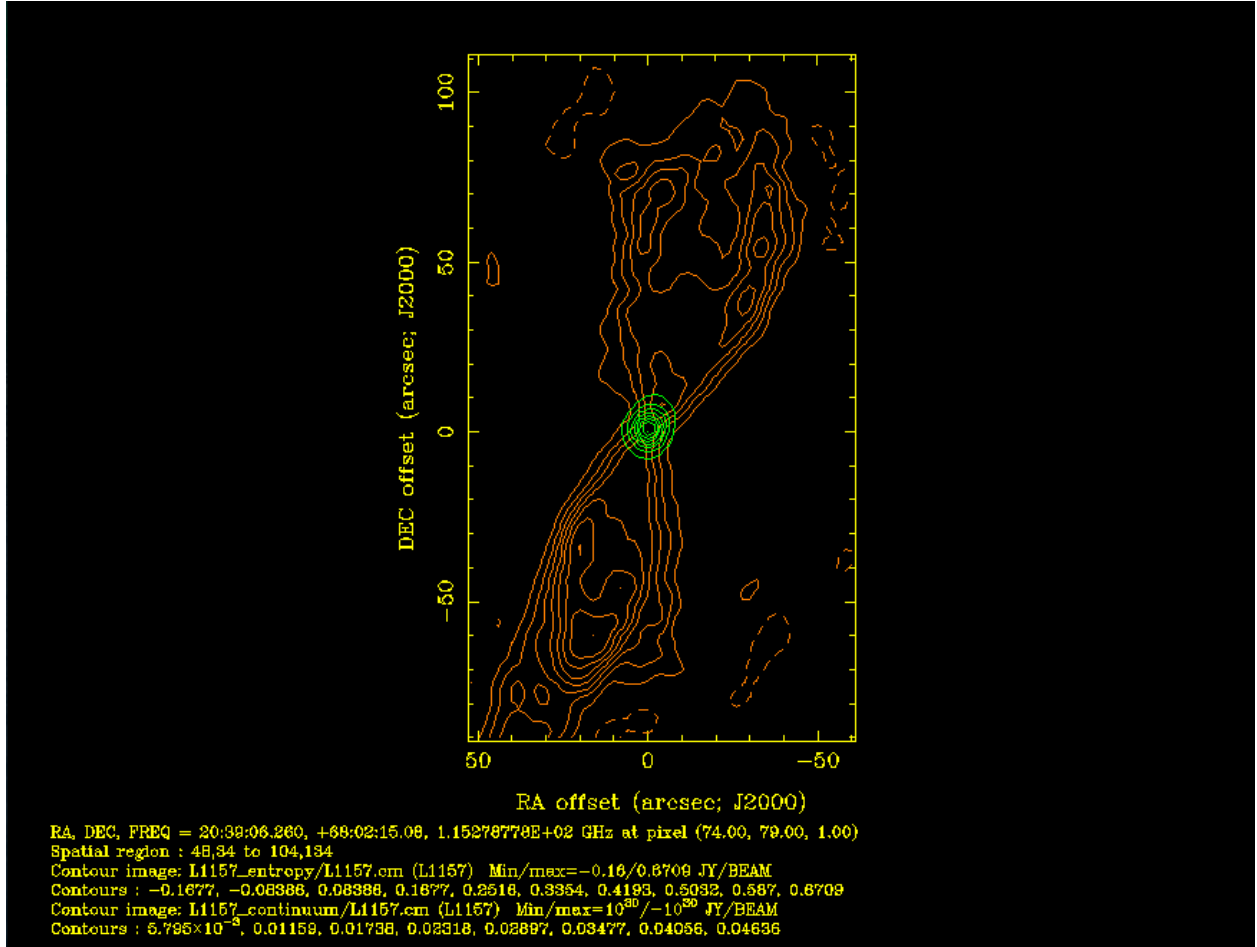


Fig. 8.— ^{12}CO (1-0) contours (red) overlaid on the continuum (green). This shows the combined envelope and outflow structure of L1157-mm.

4. Looking for Molecular Gas in NGC 1052

Lauranne Lanz (Caltech)

4.1. Introduction

4.1.1. *Molecular Gas in Elliptical Galaxies*

An important difference between spiral and elliptical galaxies is their molecular gas content. The canonical view of galaxy evolution broadly requires that gas-rich spirals eventually become, through secular or merger processes, gas-poor ellipticals. We therefore expect that there should exist transitional objects, such as ellipticals with significant molecular content. Such galaxies provide an important insight into a crucial period in galaxy evolution. The ATLAS^{3D} (Cappellari et al. 2011) sample of early-type galaxies was observed with CARMA (Alatalo et al. 2013), which showed a variety of CO morphology, including disks, spiral arms, and disturbed morphologies.

4.1.2. *NGC 1052*

NGC 1052 is a nearby ($z=0.0050$, 22 Mpc) early type galaxy with a compact, flat-spectrum radio core and a two-sided radio jet contained within the host galaxy. It belongs to a class of galaxies known as Molecular Hydrogen Emission Galaxies (MOHEGs; e.g., Ogle et al. 2010), whose mid-IR spectrum show strong H₂ emission relative to their polycyclic aromatic hydrocarbon (PAH) emission. Both PAH and H₂ emission may be excited by UV photons from young stars. However, the large ratio of H₂/PAH emission in these galaxies indicate that the energetic source of the H₂ emission cannot be star formation. Analysis of MOHEGs that are also radio galaxies (e.g., Guillard et al. 2012; Ogle et al. 2010) suggests that the most likely excitation mechanism of the molecular gas to the observed 100-1000 K temperatures are shocks driven into the interstellar medium (ISM) by the radio jets. Mapping the molecular gas using CARMA provides insights into the colder molecular gas and whether it also shows indications of interactions with the radio jet. Further, the mass and extent of the molecular gas are necessary to determine whether the radio jet has quenched star formation in this galaxy by accurately determining where on the Kennicutt-Schmidt diagram this galaxy falls.

4.2. Observations and Data Reduction

NGC 1052 was observed using the CARMA-15 subarray in the compact (E) configuration on 5 August 2014. While the optical diameter of the galaxy (69''; Wang et al. 1992) is similar in extent to the size of the 10 m primary beam, we did not expect to detect emission on the outskirts of the galaxy. Therefore, we chose to concentrate our observing time in a single pointing centered on the VLBA position of $\alpha = 02:41:04.80$ and $\delta = -08:15:20.75$ (Beasley et al. 2002). From a

single-dish observation (Nobeyama 45 m; Wang et al. 1992), we expected the ^{12}CO to be about $\sim 100 \text{ km s}^{-1}$ wide. Since we wanted to detect the structure of the line, we chose our correlator settings to balance velocity coverage and sufficient velocity resolution to detect line structure. We therefore placed a 125 MHz spectral window centered to have the ^{12}CO line in the upper side band at 115.27 GHz. Additionally, we placed three other 125 MHz spectral windows centered on the ^{13}CO line at 110.20 GHz, the CN line at 113.49 GHz, and the CS line at 97.98 GHz. We placed 250 MHz windows on the ^{18}CO line at 109.78 GHz and the CN line at 113.19 GHz. The remaining two windows were kept as 500 MHz continuum windows. The local oscillator frequency was set at 109.235 GHz.

The observation track ran for 4.8 hours. NGC 1052 was observed for hours, with the remaining time spent on calibration objects and pointing targets. Our calibration objects were: Uranus for flux, the quasar 0224+069 for gain, and 3C84 for passband. The sky was clear during the observation, but the atmosphere showed some turbulence with a typical RMS of $500 \mu\text{m}$ and $\tau_{230 \text{ GHz}} = 0.95$. The bulk of the data reduction was done using John Carpenter’s MIRIAD script. Very little flagging proved necessary. Due to the brightness of the continuum of NGC 1052, we elected to self-calibrate the passbands rather than using 3C84, which also showed greater amplitude variations. Additionally, we chose to use natural weighting since the source did not appear particularly extended.

4.2.1. Ancillary Data

We wanted to determine where the sub-millimeter emission fell relative to the stellar, dust, hot gas, and radio jet emission of NGC 1052. For the stellar emission comparison, we obtained a g -band image from the SDSS DR10 archive. We were in possession of a $70 \mu\text{m}$ image taken with the PACS instrument on the Herschel Space Observatory. This mosaic was created using the software Scanamorphos (Roussel 2013) from data in the Herschel Science Archive. For the hot gas comparison, we reprocessed the Chandra X-ray Observatory observation taken from the Chandra Archive using the CIAO software (v. 4.5; Fruscione et al. 2006). A Very Large Array image taken as part of the FIRST survey was also acquired (D. Crichton, priv. comm.).

4.3. Results and Discussion

4.3.1. 3mm Continuum

NGC 1052 has very bright 3 mm continuum emission of $0.97 \pm 0.03 \text{ Jy}$. Figure 9 shows the image created from the data of one of the broad continuum windows. The overlaid contours shows the ellipse fit to it with the MIRIAD task *imfit*. This task determined that the continuum emission is well-modeled as a point source, with a FWHM of $10''.8 \times 7''.0$, very similar to the beam shown in the bottom right.

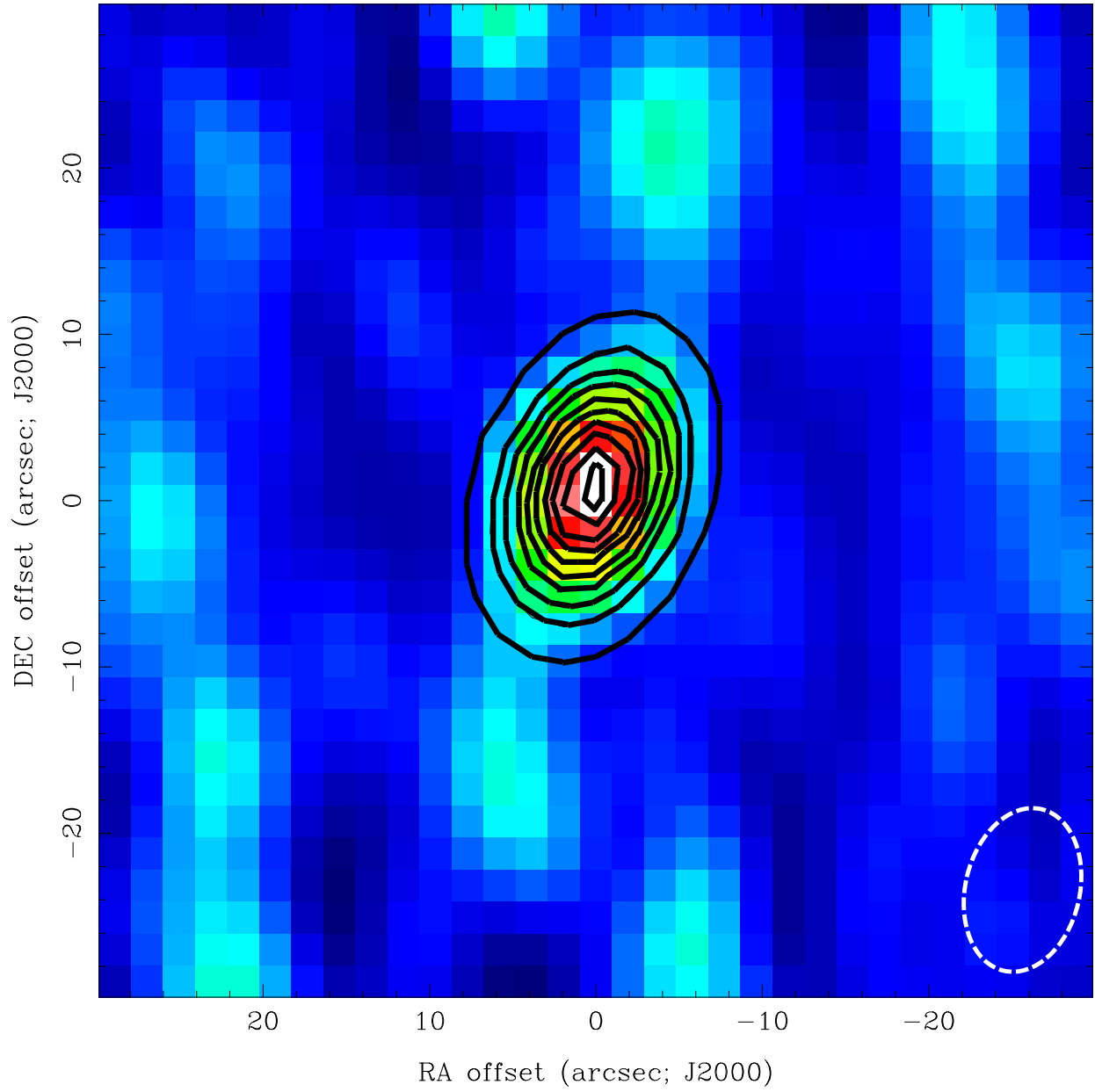


Fig. 9.— Continuum map of NGC 1052 overlaid with contours derived by *imfit*, showing the emission to be point-like.

In extragalactic observations, $10''$ can extend across much of a distant galaxy or describe the very center of a galaxy. As such, we want to establish whether a submillimeter source unresolved with this configuration of CARMA is confined to the nuclear region or could extend over a significant fraction of the galaxy. Figure 10 overlays the contours of SDSS g -band emission showing the stellar extent (Fig. 10a), the PACS $70\ \mu\text{m}$ emission showing the dust (Fig. 10b), the broadband (0.5–8 keV) Chandra emission showing the AGN and hot gas emission (Fig. 10c), and the VLA emission showing the radio jets (Fig. 10d). These images demonstrate that the submillimeter emission is confined to the central region of the galaxy and, may well be associated with the AGN. Fig. 10c in particular shows that the submillimeter and central X-ray point source are spatially coincident. Similarly, the positions of the radio core and continuum point source agree.

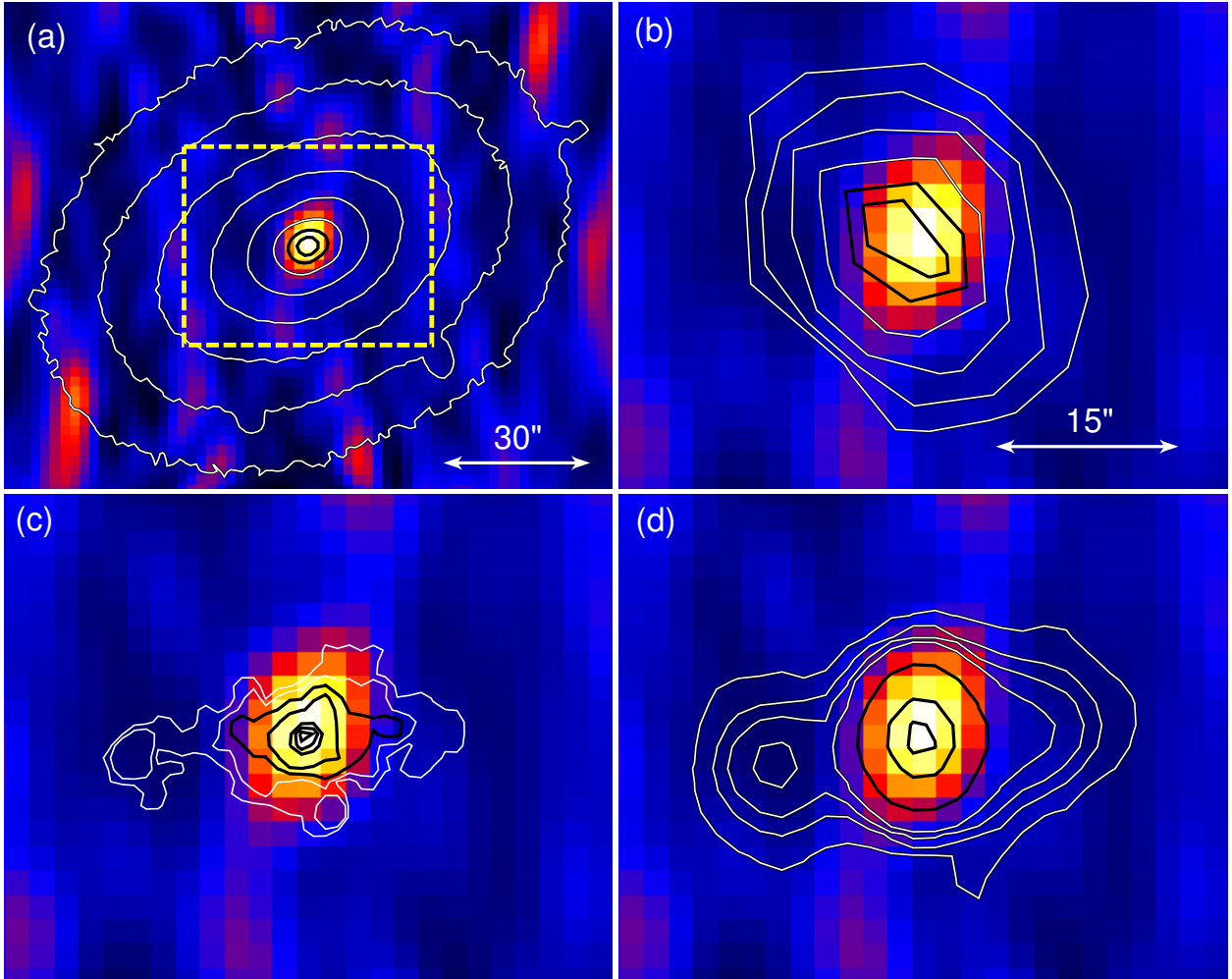


Fig. 10.— Continuum map of NGC 1052 overlaid with contours from (a) SDSS g , (b) PACS $70\ \mu\text{m}$, (c) Chandra 0.5–8 keV, and (d) VLA 1.4 GHz. The latter three are on a smaller scale within the yellow box shown in (a). The mix of black and white contours is purely to improve visibility.

4.3.2. $^{12}\text{CO}(1-0)$ Emission

We tried two methods for detecting the $^{12}\text{CO}(1-0)$ line. First, we extracted the spectrum in the clean map of the spectral window containing the $^{12}\text{CO}(1-0)$ line using *imspec* and subtracted the continuum determined from the average of the channels on both sides of the expected position of the lines. The result is shown in Figure 11. While there exists a spectral feature at the velocity expected from the Nobeyama observation (Wang et al. 1992), the fact that it is only the width of one 8 km s^{-1} channel is concerning. Therefore, we tried a second extraction method, wherein we subtract the average of the dirty maps in the wide continuum windows from the dirty map of the $^{12}\text{CO}(1-0)$ window. This subtraction must be done with the dirty maps rather than the cleaned maps, because the deconvolution process used in cleaning is non-linear. Since the two sets of dirty maps should have similar side lobe features, the subtraction will also do a simple cleaning on the spectral map. Indeed, we find that the maps of the continuum windows are have very little in the way of residuals once their average is subtracted from them. We extracted the spectrum in the subtracted map and find a spectrum very similar to that shown in Figure 11. At this time, whether emission in the $^{12}\text{CO}(1-0)$ line has been significantly detected remains unclear. However, if the spectral feature seen in Figure 11 does accurately reflect that emission, then it has a similar spatial morphology to the continuum, albeit a much weaker detection.

4.3.3. Future Work

An important lesson learned from this project is that, for extragalactic observations, the correlator spectral windows are best kept at 500 MHz. We obtained a second observation of NGC 1052 just after the end of the CARMA school on 9 August 2014, with better correlator settings, with which we hope to significantly detect the ^{12}CO line.

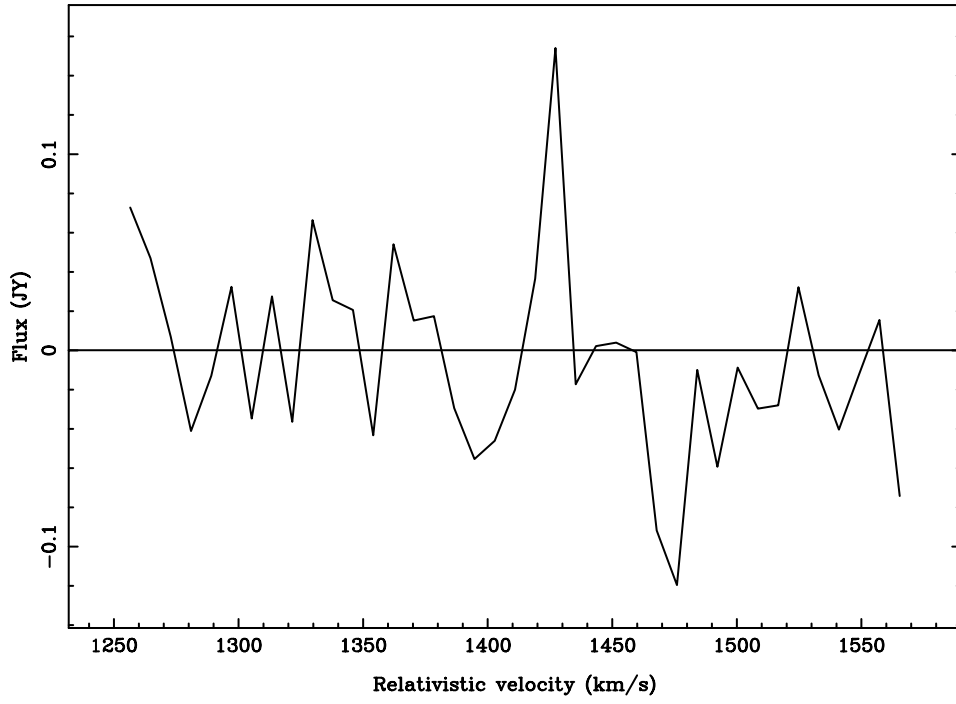


Fig. 11.— Continuum-subtracted spectrum in the $^{12}\text{CO}(1-0)$ window.

5. Millimeter Observations of RW Aurigae: Searching for Disrupted Circumstellar Material

Joseph E. Rodriguez Jr. (Vanderbilt University)

5.1. Introduction

The circumstellar environment of young stellar objects (YSOs) involves dynamical interactions between gas and dust. The gas and dust typically orbit in a circumstellar disk, and can be inferred by an excess of infrared radiation. Observing the environment of YSOs and how the gas and dust interact, can provide us with crucial information to better understand the processes of planetary formation. An extreme example of a YSO environment is the classical T-Tauri star, RW Aurigae. Cabrit et al. (2006) performed millimeter observations of the RW Aurigae system, providing evidence that the system had undergone a reconfiguration of its circumstellar environment. As RW Aur B orbited close to the primary component, RW Aur A, it disrupted the surrounding circumstellar material of RW Aur A. This material has now co-alesed into a large tidal arm, wrapped around RW Aur A (Figure 12). In 2010, the system dimmed by ~ 2 magnitudes (in the V -band) for a duration of 180 days (Figure 13). It is believed that this dimming was caused by a portion of disrupted material, from the system’s violent history, occulting the RW Aur A (Rodriguez et al. 2013).

The Rayleigh-Jeans approximation, $F_\nu \sim \nu^{2+\beta}$, allows us to combine the measured total flux in millimeter observations to infer properties of the circumstellar environment of RW Aurigae. If β is measured to be around 2, this is indicative of an optically thin disk and likely no grain growth. If β is less than 1, this suggests the circumstellar material is optically thick and possibly undergoing grain growth through collisions.

5.2. Observations and Data Reduction

We observed the RW Aurigae system using the Combined Array for Research in Millimeter Astronomy (CARMA) for ~ 3.2 hours. Specifically, we used the CARMA 15 E configuration consisting of nine 6.1m and six 10.4m antennas. All observations were taken on August 7th, 2014 between Local Sidereal Time 0h and 5h. Along with observing RW Aurigae, we observed Uranus, 3C84 and 0510+180 as the flux, passband and gain calibrator, respectively. Due to inadequate weather for 1mm observing, we observed in the 3mm continuum. The observations and maps presented here were reduced using the MIRIAD software program, described in detail by Sault et al. (1995).

5.3. Results and conclusion

Using the CARMA 15 E array, we hoped to accomplish a few goals along with the learning experience that the CARMA summer school provided. First, we would like to expand on the IRAM

1.3mm map that Cabrit et al. (2006) presented, looking for previously undetected material. Second, combining our observations with previous mm observations, we are able to tentatively interpret the presence of grain growth.

In Figure 14, both the dirty and clean 3mm maps are presented. By “Dirty Map”, we are referring to the uncalibrated, unprocessed, raw data that is outputting but the array. The “Clean Map” has been fully calibrated and poor data has been flagged and removed from the reduction. The clean map shows a clear detection of the RW Aur system. Figure 15 presents the final cleaned map, using a color scaling to show the true contours of the detection. This plot is also zoomed in to show the nearby area surrounding the RW Aur system. In our final map, we clearly detect RW Aur but only as a point source. There appears to be some elongation but this is not statistically significant when compared to the beam size.

We are able to calculate the total flux of RW Aur in the 3mm continuum to be 6.24 ± 0.2 mJy. Previous results by Cabrit et al. (2006) measured a total flux in the 1.3mm band to be 32.8 ± 0.7 mJy with $0.89''$ resolution. Osterloh & Beckwith (1995) found the 1.3mm flux to be 42.5 ± 5 mJy with a $12''$ beam. Keeping the beam sizes consistent, we combine our measurements here with the Osterloh & Beckwith (1995) measured flux to estimate the value of β in the equation presented above. We calculate that $\beta \sim 0.25 \pm 0.2$. Even though the error on our observations is quite high, our value of β is consistent with an optically thick disk and may indicate the presence of grain growth. If the proposed violent history of the RW Aur system is correct, that RW Aur B is on an eccentric orbit and during the last fly-by it significantly disrupted the circumstellar material around RW Aur A, it would likely increase the amount of grain collisions. Therefore, it is possible that the interaction increased grain growth and our calculated value of β is indicative of that. However, we can not claim the presence of grain growth without more definitive results.

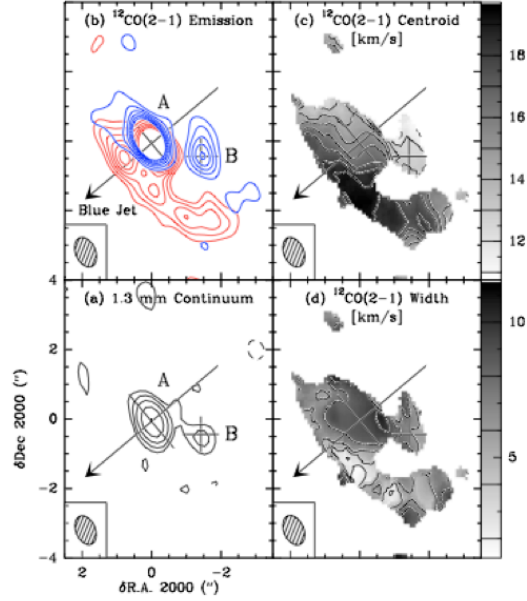


Fig. 12.— Figure 1 from Cabrit et al. (2006) showing the a) $^{12}CO(2-1)$ emission, b) $^{12}CO(2-1)$ centroid, c) 1.3mm continuum and d) $^{12}CO(2-1)$ width maps of the RW Aurigae system from IRAM.

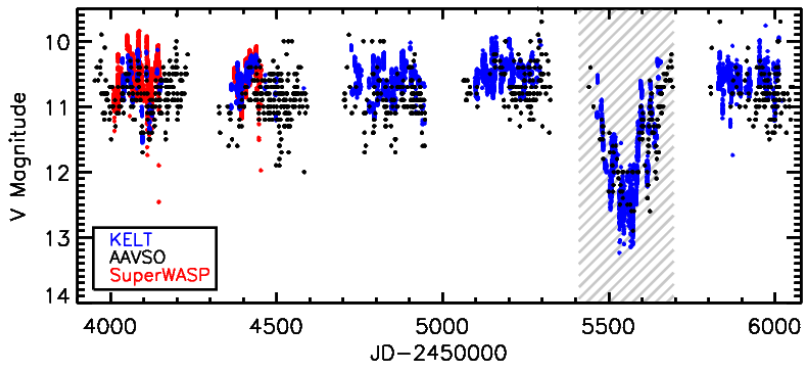


Fig. 13.— Figure 1b from Rodriguez et al. (2013) showing a large dimming event from 2010 to 2011. Plotted are the KELT-North, SuperWASP and AAVSO light curves from the KELT-North observing seasons.

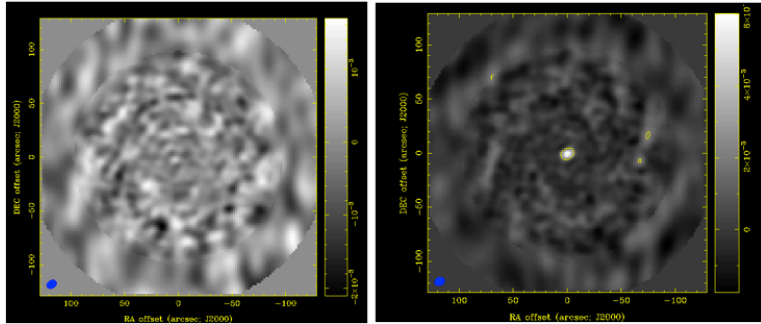


Fig. 14.— The dirty map and clean map of the 3mm RW Aurigae observations. The beam size is shown in the bottom left corner.

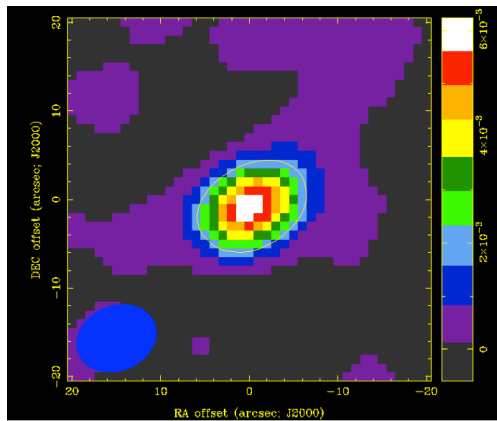


Fig. 15.— The final clean map of the 3mm RW Aurigae observation, colored to show the gradient of flux detected. The beam size is shown in the bottom left corner.

6. CO emission in the famous dwarf irregular galaxy IC 2574

Ned Molter (Macalester College) and Amy Steele (University of Maryland)

6.1. Introduction

The low mass and metallicity of dwarf galaxies make them local analogs to galaxies at high redshift, meaning that studying the local dwarf galaxy population is essential to understanding galaxy formation and evolution in the early Universe. In particular, star-forming dwarf irregular galaxies aid our understanding of the way star formation proceeds in the low metallicity regime, where gas clouds are less abundant in heavy molecules like CO. The tight relationship between molecular gas and star formation (Bigiel et al. 2008) suggests that such molecules play an essential role in radiating energy out of a molecular gas cloud, cooling it and allowing it to collapse. However, gas cloud collapse and star formation must also have occurred in Population III stars with zero metallicity, and the details of this process are constrained only theoretically—no empirical evidence exists. Metal-deficient dwarf galaxies are therefore a crucial test bed for star formation processes at low metallicities.

IC 2574 (see Figure 16) is a very famous example of a fairly low-mass, metal poor galaxy, with over 370 references to it in the NASA Extragalactic Database. It has a metallicity of $12+\log(\text{O}/\text{H}) \approx 8.15$ ($\approx 30\% Z_{\odot}$ Miller & Hodge 1996), and an HI mass of $1.4 \times 10^9 M_{\odot}$ (Walter & Brinks 1999) at an adopted distance of 3.94 Mpc (Melbourne et al. 2012). This galaxy is particularly interesting because of the structure in its HI gas distribution, which reveals 48 holes ranging in size from 100 pc to 1000 pc (Walter & Brinks 1999). These features are likely to form when an episode of vigorous star formation produces young massive stars whose stellar winds and type II supernovae provide enough mechanical energy to drive away gas and sometimes trigger secondary star formation on the edges of the newly-formed shells. The largest (supergiant) shell in IC 2574 provides a textbook example of triggered star formation around an HI shell (Weisz et al. 2009). Shells are most easily studied in dwarf galaxies because dwarfs undergo solid body rotation; the lack of shear in the disk allows structures to persist for longer than in disk galaxies.

Star formation relies on the presence of molecular gas, but molecular gas clouds had not previously been studied in detail in this galaxy. A single pointed observation with the ARO Kitt Peak 12m telescope (Leroy et al. 2005) reports a point-source detection of CO (1-0) in the galaxy’s center with an intensity of $I_{CO} = 0.83 \text{ K km s}^{-1}$ over a beam area of $55''$ (see Figure 17 for the detection spectrum). A follow-up observation by the IRAM 30m telescope in CO (2-1), however, reports a non-detection (Leroy et al. 2009). This interesting discrepancy means that the gas cloud or clouds at the ARO 12m pointing are probably very dense, causing the molecular component to remain very cool and preventing strong emission from higher-energy transitions. We therefore carry out a more detailed study of the molecular gas in IC 1574 at 115 GHz with CARMA, the first attempt at such an observation with an interferometer.

6.2. Observations and Results

We observed the center of IC 2574 for a total time of ≈ 10 hours. The 60" CARMA15 field of view completely covered the $\approx 55''$ ARO 12m telescope's beam. Our correlator setup achieved a velocity resolution of 0.6 km s^{-1} in the range -20 km s^{-1} to 140 km s^{-1} , covering the entire velocity range where CO emission was found in the previous detection. Our two observing tracks, both taken in the late morning to early afternoon, gave us a combined on-source time of ≈ 10 hours. Unfortunately, the data was compromised by bad weather: one track received a weather grade of C and the other a grade of D. The CO emission line was affected the most strongly, as it is found near to the 118 GHz oxygen line.

Standard reduction techniques were performed on the data using the MIRIAD software package. Our final unaveraged data cube displayed an RMS noise level of $248 \text{ mJy beam}^{-1}$ at a line width of 62 MHz and a beam size of $7.28'' \times 6.66''$. This is over six times noisier than predicted by the CARMA sensitivity calculator, which expected a noise level of $42.9 \text{ mJy beam}^{-1}$ at the same line width under normal weather conditions. We attribute this discrepancy to the bad weather. We also created data cubes with channels averaged to 2, 5, 10, 20, 40, 60, and 80 km s^{-1} velocity resolution. We do not detect significant CO emission from the galaxy in any of our cubes.

6.3. Discussion and Conclusions

The Leroy et al. (2005) CO (1-0) detection reports an intensity of $I_{CO} = 0.86 \pm 0.17 \text{ K km s}^{-1}$, or $27.3 \text{ Jy km s}^{-1}$. Their spectral line width is published only graphically, but we estimate it to be at most 80 km s^{-1} . This translates to a flux of 341 mJy across a 55" beam. If we average our channels to a velocity resolution of 20 km s^{-1} to better compare with the Leroy et al. spectrum, our RMS noise becomes 35.9 mJy. Despite the bad weather, these numbers suggest that if the source were a single point source it should have been detected. It is therefore likely that the Leroy et al. $\approx 55''$ beam actually covers more than one cloud of molecular gas hiding just below our current noise threshold. This prediction is supported by the distribution of $H\alpha$, a tracer of ongoing star formation, in Figure 16d. The image shows multiple knots of star formation within CARMA's $\approx 60''$ field of view at our pointing, and since molecular gas is associated with star forming regions, it is likely that the CO emission would appear as multiple point sources as well.

To conclude, due to bad weather we did not confirm the detection of CO in the famous metal-deficient dwarf galaxy IC 2574, previously detected by the Kitt Peak ARO 12m single dish telescope. Comparing our RMS noise threshold with the intensity of the CO emission found by the previous detection, we conclude that if the molecular gas in IC 2574 were a point source to our $\approx 7''$ beam, we would have detected it. We interpret this finding, coupled with the $H\alpha$ detection of multiple star forming regions within the ARO 12m telescope's beam, as evidence that the molecular gas in IC 2574 is extended over a large area, making it difficult to detect with CARMA's higher spatial resolution.

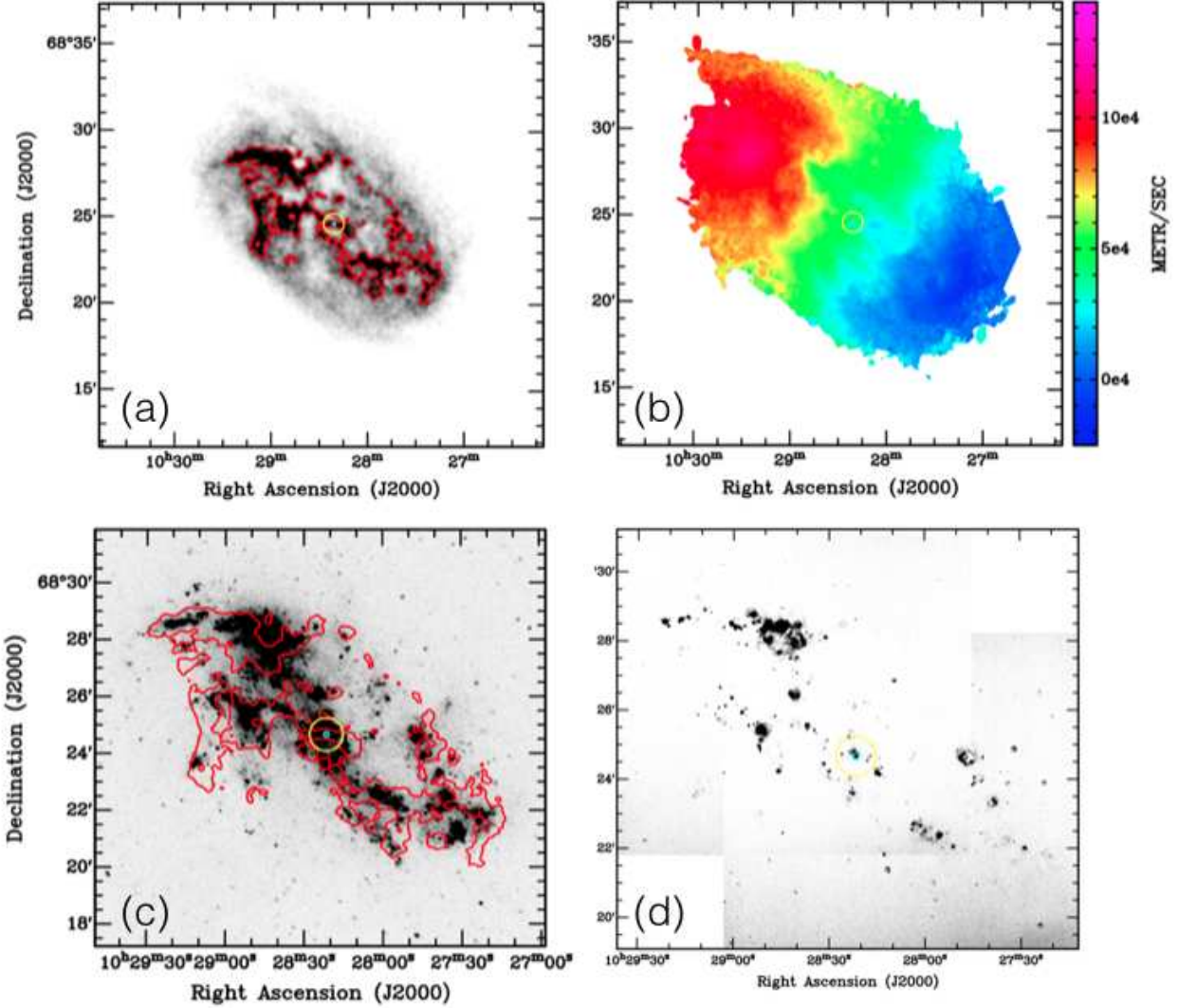


Fig. 16.— (a) HI column density image of IC 2574 at 12'' resolution (Walter et al. 2008). The red contour is shown at the $1.4 \times 10^{21} \text{ cm}^{-2}$ level. (b) Intensity weighted velocity field of IC 2574 at 12'' resolution. (c) Archival GALEX FUV image of IC 2574, with the red HI contour at 1.4×10^{21} atoms cm^{-2} overlaid from panel (a). (d) Archival Kitt Peak 2.1m telescope H α image of IC 2574 (Lee et al. 2007). The 60'' CARMA field of view is denoted by the yellow circle near the center of each image, and the 6'' beam is represented by the small blue circle inside it. The fields of view of panels (c) and (d) differ slightly from those in panels (a) and (b).

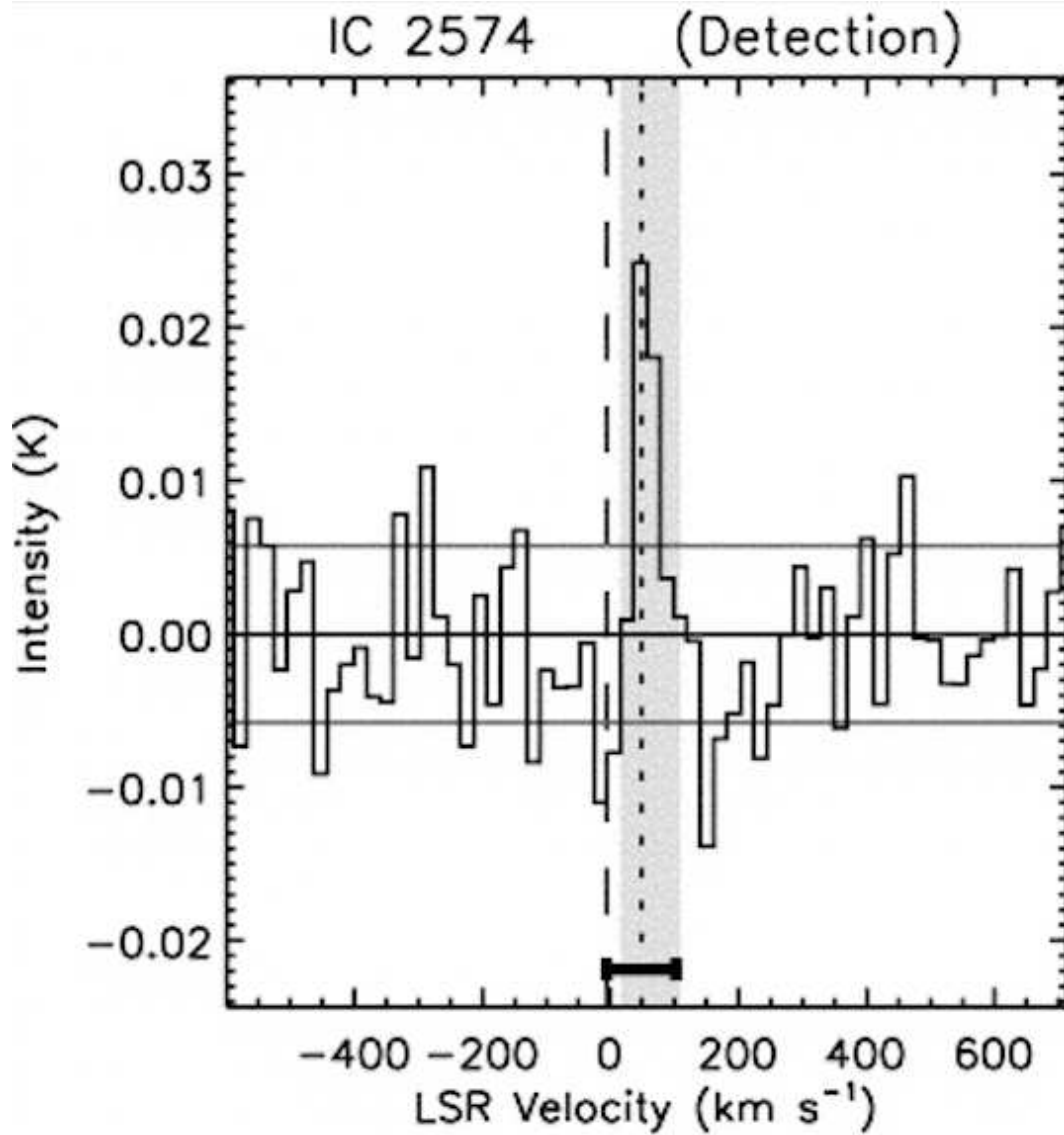


Fig. 17.— Spectrum of the ARO 12m single-dish point source detection of CO (1-0) in the center of IC 2574 (Leroy et al. 2005). The reported integrated CO intensity within the telescope’s 55” beam is 0.83 K km s^{-1} . This translates to a flux of 0.34 Jy at a line width of 80 km s^{-1} or 0.68 Jy at a line width of 40 km s^{-1} .

7. Sunyaev-Zel’dovich Observations of the ZW3146 Galaxy Cluster Jonathan Florez (Fisk University) and Devin Crichton (Johns Hopkins University)

7.1. Introduction

In the past couple of decades the quality of Sunyaev-Zel’dovich Effect (SZE) observations have increased drastically due to the development of radio interferometers that have improved low-noise detectors and systematics. Such instrumental developments have allowed us to study the hot intracluster medium (ICM) gas of galaxy clusters, ranging in mass from 10^{14} – 10^{15} M_{\odot} , across a wide spectrum of angular scales (Carlstrom et al. 2002). The SZE produces inverse Compton scattering of CMB photons on the hot electron gas of the ICM, making it a useful tool in the study of the massive galaxy clusters and their baryonic content. Current observations of galaxy clusters have shown that a great deal of clusters in similar mass ranges have a hot ICM gas that emits X-rays (De Lucia et al. 2004). As a result, SZE and X-ray observations complement each other very well and give us multiple ways to probe the ICM gas of massive clusters. A detailed study of combined SZE and X-ray data will allow us to better understand certain physical processes driving the evolution of such massive clusters (Zhang & Wu 2000).

Our target for the CARMA 2014 Summer School was ZW3146, a galaxy cluster at $z = 0.291$ that has high X-ray emission (Mushotzky & Loewenstein 1997) and is massive enough to produce flux decrements in the CMB map at 30 GHz. These flux decrements, due to the SZE, became visible after ~ 10 hours of observations and required detailed reduction and faulty data flagging. We collected ~ 17 hours of observations at 30 GHz using the Sunyaev-Zel’dovich Array (SZA) at CARMA and acquired a significant detection after modeling and removing two point sources from the field of view. SZE observations of ZW3146 combined with existing X-ray and lensing data will allow us to better understand the three-dimensional structure of the dark matter halo of this cluster and the physics of its ICM.

In this report we provide a brief introduction to the SZE, describe our observations of the SZE of ZW3146 during the CARMA Summer School 2014, detail the data reduction methodologies we used on the data thus acquired and conclude with an description of the results.

7.2. Sunyaev-Zel’dovich Observations of Galaxy Clusters

The relic thermal radiation from the big bang, which we observe today as the cosmic microwave background (CMB), provides a useful backlight that we can leverage to probe the intervening structures in the universe. The Sunyaev-Zel’dovich Effect (SZE, Sunyaev & Zeldovich 1980) refers to the inverse Compton scattering of the CMB photons by hot plasmas such as the gravitationally shock-heated gas residing in the dark matter halos of galaxy groups and clusters as shown schematically in Figure 18. This imprints a characteristic spectral distortion on the thermal spectrum of the primordial CMB signal. The lower energy CMB photons passing through such a pocket of hot

plasma have a small ($\lesssim 1\%$) chance of being up-scattered to higher energies by interactions with the more energetic ions. When we measure the microwave sky in the direction of these structures, we observe a decrement in the CMB signal at frequencies below ~ 220 GHz and a corresponding increment at higher frequencies.

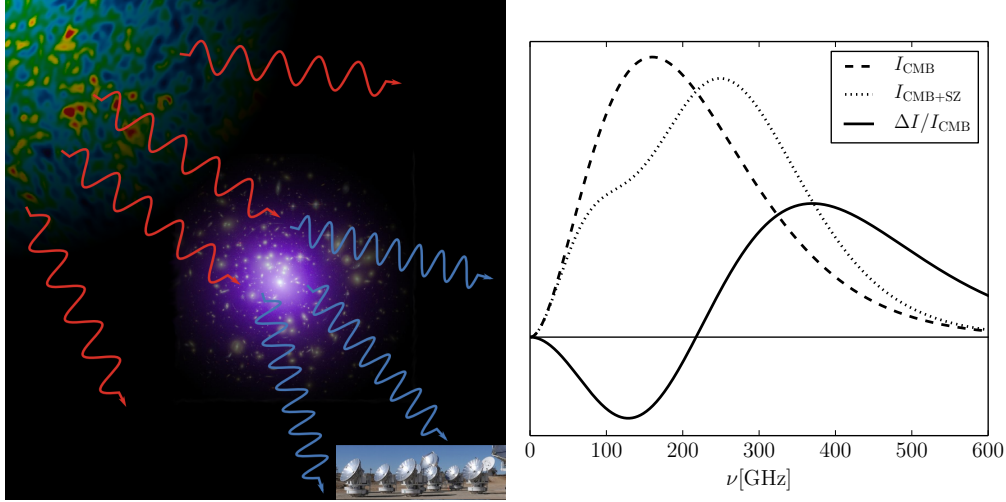


Fig. 18.— *Left*: A schematic diagram demonstrating the origin of the SZ effect; Low energy photons from the CMB are scattered to higher energy through inverse Compton scattering with the hot ions in the intracluster medium. *Right*: The spectral signature of the SZ effect. The dashed and dotted lines show, in flux density units, the blackbody CMB spectrum with and without a distortion from the SZ effect, respectively. The solid line shows the relative difference between these spectra and reflects the effective spectrum of the SZ effect as observed.

The SZ signal is thus observed as a frequency dependent distortion of the CMB intensity:

$$\frac{\Delta I_\nu}{I_{\text{CMB}}} = y g(\nu); \quad y = \frac{\sigma_{\text{T}}}{m_e c^2} \int n_e T_e dl \quad (1)$$

$$g(x(\nu)) = \frac{x^4 e^x}{(e^x - 1)^2} \left(x \frac{e^x + 1}{e^x - 1} - 4 \right). \quad (2)$$

Here, y is known as the Compton parameter and is proportional to the integral of the electron number density, n_e , multiplied by the electron temperature, T_e , along the line of sight. This quantity is therefore a measure of the integrated thermal pressure of ionized gas along a given direction in the sky. In the non-relativistic limit, the spectral distortion function, $g(\nu)$, depends only on the dimensionless frequency, $x \equiv h\nu/k_{\text{B}}T_{\text{CMB}}$. The shape of this distortion is shown in Figure 18.

Massive clusters have $y \gtrsim 10^{-4}$ and, with $I_{\text{CMB}} \equiv 2(k_{\text{B}}T_{\text{CMB}})^3/(hc)^2 = 270$ MJy/sr and $g(\nu = 30 \text{ GHz}) \approx -0.5$ we expect to see a decrement signal on the order of 1 mJy/arcmin². This in turn should produce a signal of a few mJy/beam given the $\sim 100''$ beam of the compact subarray of CARMA-8. This signal should be extended on the $> 1'$ angular scales typical of a cluster.

An important characteristic of the SZE is that, since it is a scattering process, the surface brightness of the signal does not suffer from the same cosmological dimming with distance that is seen in emission processes. This makes the SZE a useful tool for probing the distant universe. Furthermore, the integrated SZ signal attributed to a cluster is related to the total thermal pressure of the ICM gas that it hosts. Under the assumption of hydrostatic equilibrium the integrated SZ effect of a cluster is therefore expected to be a good proxy for its mass (Motl et al. 2005). The SZE may therefore be used to trace the growth of structure in the universe over cosmological time scales, providing constraints on cosmological parameters such as the amplitude of the matter power spectrum, σ_8 , and the fraction of the critical density of the universe attributed to matter, Ω_M . However, in practice, our ignorance of the details of the distribution of thermal pressure within galaxy clusters as well as deviations from hydrostatic equilibrium in the ICM systematically limit such studies (e.g., Hasselfield et al. 2013). Finer observations of the SZE over a wide range in angular scales such as those provided by interferometers are therefore crucial in enhancing precision cosmology with the SZE.

7.3. CARMA-8 Observations of ZW3146 at 30 GHz

For our observations, we used the CARMA-8 (SZA) mode of the array, utilizing the 3.5m telescopes for continuum observations at 1cm. For this purpose, the correlator was setup in the wideband mode and observations were scheduled for a single on target pointing with no mosaicing. In each cycle we alternated between integrating for 15 minutes on our target and 3 minutes on our calibration source, 1058+015. As this is a >5 Jy source, it was used as both as a gain and passband calibrator. For flux calibration we observed Mars at the end of each of our observing runs which took place from 8/5/2014–8/9/2014. During this time ZW3146 was transiting at roughly 2PM local time, with a total up time of approximately 7 hours. Due to inclement weather on 8/5/2014, we have not used the data taken on that day in this study. A summary of the observations used for this project is shown in Table 1. The total on target integration time in the raw data is ~ 17 hours.

Table 1: Summary of observations carried out during the summer school.

Observation Date	Quality Grade	Source integration time [hours]	Sky RMS range [μm]	τ_{230} range
8/6	A+	3.74	500–800	0.5–0.8
8/7	A+	3.16	500–1500	0.5–0.8
8/8	A+	5.14	200–800	0.4–0.6
8/9	A+	4.71	200–1000	0.4–0.8

After acquiring the data, we independently flagged each day’s visibility datasets, primarily focusing on spurious signals in some correlator windows and periods of system temperature or sky RMS

spikes. We used John Carpenter’s scripts¹ to facilitate this process. The flagged and calibrated data were then combined using the *uvcat* tool and clean images from the full dataset were produced using the *mossmi* routine. The final clean and dirty maps are shown in Figure 19

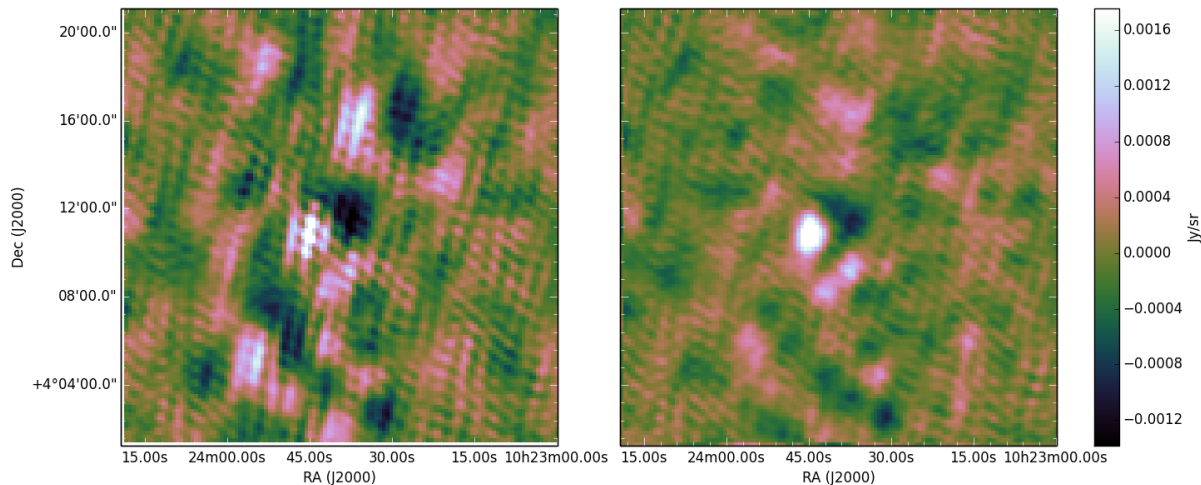


Fig. 19.— Dirty (left) and clean (right) images of ZW3146 using all the data acquired during the summer school, after flagging.

7.4. Point Source Subtraction

Within the observed field of view of the cluster lie two radio galaxies identified in the NVSS (NRAO VLA Sky Survey) at 1.4 GHz (Condon et al. 1998) and previously observed in 30 GHz studies of this cluster (Coble et al. 2007). Radio galaxies such as these appear as point sources in our data (Figure 20) and emit at 30 GHz, acting to fill in the expected decrement signal of ZW3146. Since this reduces the significance of the SZE detection and distorts the shape of the SZE signal, we modeled the sources present in our data and subtract them from our reduced dataset.

We use the Difmap package, a program developed for the synthesis imaging of data from radio interferometer arrays (Taylor 1997), to model the point sources in our field of view. Difmap offers unique mapping and interactive processing techniques that allow one to view and model the data at different angular scales. In Difmap, one can load the visibility data and specify which baselines to work with. The first step to modeling the point source in Difmap is to make a uvf file from the combined reduced miriad data extracting only ZW3146 as the object of interest. The next step is

¹http://carma.astro.umd.edu/carma/summerschool/2014/carma_calibrate.csh

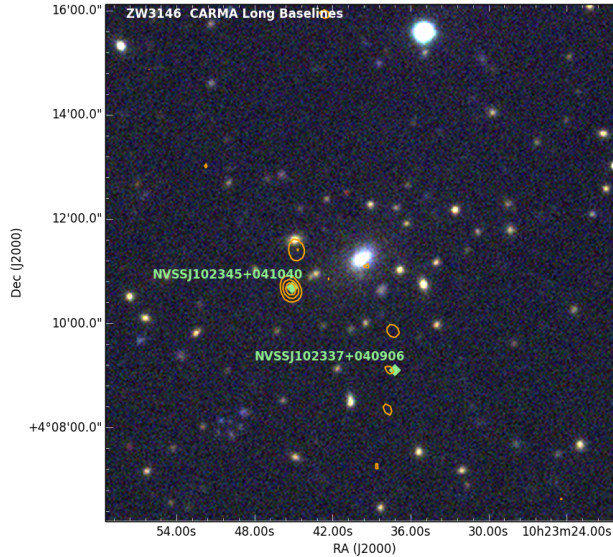


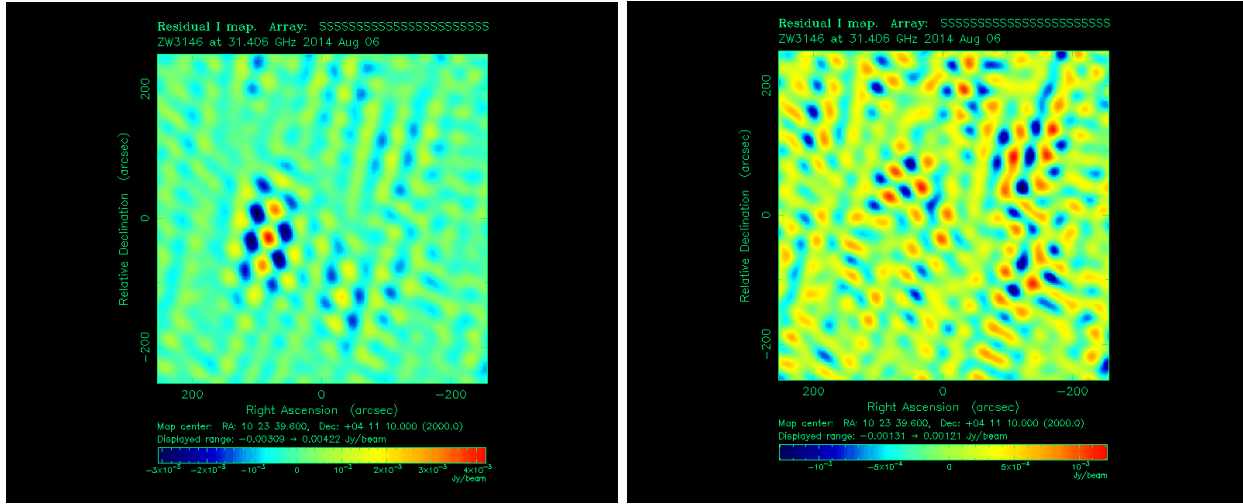
Fig. 20.— Locations of NVSS point sources in the field overlaid with signal to noise contours of the reduced CARMA-8 data which has been cut to display only the long baselines to the out-rigger antennas 18 and 19. The optical image is derived from optical SDSS observations of ZW3146 in the i , r and g bands.

to load the long baseline visibility data into Difmap to get a view of the residual map. A 4.2 mJy source is strongly visible at roughly 100 arcseconds from the target center. A second, less noticeable point source is located slightly southeast of the image center and exhibits a flux of roughly 2 mJy. Using a command in Difmap known as ‘modelfit’ one can model point sources and subtract them from the long baselines. After subtracting the point sources from the field of view we are left with what looks like noise in the residual map. The long baseline map before and after the subtraction can be seen in Figure 21.

7.5. Results and Conclusions

We present our map of cluster ZW3146 in Figure 22 after the point sources have been subtracted in the long baselines. Once again we use Difmap to read in the short baseline visibility data. The cluster clearly exhibits a flux decrement near the center of the map, at -4 mJy/beam. The cluster signal of the SZE appears roughly 100 arcseconds in diameter, with the peak slightly off center. The flux decrement exhibited by the cluster only becomes significant after ZW3146 acquires over 10 hours of integration time.

We observed ZW3146 for 17 hours to get the result we present in this memo. We find that in order to acquire any good visibility data we must flag out any bad channels and antennas, as well as throwing out any data that may have been acquired during bad weather. Point source subtraction



(a) Long baseline data before point source subtraction (b) Long baseline data after point source is removed

Fig. 21.— The long baseline visibility data displayed in Difmap. A point source can be seen in the first map, at ~ 100 arcseconds to the left of the image center. Another point source, slightly harder to detect, is noticeable also ~ 100 arcseconds southeast of the map center. After modeling the point sources and removing them we get the resulting residual map on the right which looks like noise, i.e. there are no other sources apparent.

is also an important part of the process prior to viewing the full SZ signal, as flux from the point sources can interfere with the short baseline visibility data. The resulting data is a uvf file that can be used to acquire important information about the cluster, such as its characteristic physical scale, R_{500} and Compton- y parameters, which can in turn teach us about the physics of the hot ICM gas.

8. CO Observations of the Host Galaxy of Broad-lined Type SN Ic 2005ks Patrick Kelly (University of California, Berkeley)

8.1. Introduction

The supernovae (SN) associated with long-duration gamma-ray bursts (LGRBs) are broad-lined Type Ic (Ic-BL) explosions, whose spectra exhibit wide features consistent with ejecta velocities of $\sim 0.1c$. In a recent paper Kelly et al. (2014), we showed that the host galaxies of SN Ic-BL and LGRBs have high stellar-mass and star-formation densities, in comparison to SDSS galaxies that have similar stellar masses (see Figure 23). Core-collapse SN having typical ejecta velocities, however, do not exhibit any preference for overdense galaxies. This suggests that star formation must proceed differently in the overdense host galaxies of SN Ic-BL and LGRBs.

My CARMA summer school project was to measure or constrain the molecular hydrogen content of the host galaxy of SN 2005ks, a nearby $z = 0.098$ broad-lined SN Ic. This measurement is a necessary step (along with HI host galaxy measurements) to being able to determine whether star formation is consistent with the Kennicutt-Schmidt relation between star-formation density and gas density Kennicutt (1998); Schmidt (1959). Given the ability to detect LGRBs at high redshift, they may become important tracers of star formation in low-luminosity galaxies too faint to be detected even by e.g., Giant Magellan Telescope, and the Thirty Meter Telescope.

A color composite image of the $z = 0.098$ host galaxy shown in Figure 24. The star-formation density of the host galaxy of SN 2005ks is $10^{-1.17 \pm 0.14} M_{\odot} \text{ yr}^{-1} \text{ kpc}^{-2}$.

8.2. Observations and Data Reduction

We obtained a 5.7 hr integration centered on the host galaxy coordinates $\alpha = 21:37:56.52$ and $\delta = -00:01:57.64$ in the CARMA 15-antenna compact E configuration in favorable atmospheric conditions. During the track, $\tau \approx 0.81$ and the phase rms was $205 \mu\text{m}$. We observed the $^{12}\text{CO}(1 - 0)$ emission line at 115.27 GHz. From the spectroscopic galaxy redshift available from the SDSS survey², we calculated that this transition has an observer frame frequency of 104.92 GHz. We configured the correlator to bracket this frequency with a 250 MHz band, and placed seven additional 250 MHz bands adjacent in frequency to this center band.

The data were reduced using the sequence of steps in the MIRIAD script provided by John Carpenter. Several antennas were not functioning properly and were removed, but the data required minimal flagging. We extracted a spectrum within a $5''$ square aperture positioned at field center that contains the host galaxy optical emission.

²<http://skyserver.sdss3.org/public/en/get/SpecById.ashx?id=4723347288133992448>

8.3. Results and Discussion

As the extracted spectrum in Figure 25 shows, we do not detect ^{12}CO emission from the host galaxy. To determine an upper limit on the line strength from the data, we measure the rms scatter in the background and the expected width of the line from the nebular lines present in the SDSS optical galaxy spectrum. We convert the line strength flux limit to a constraint on the mass of molecular hydrogen using the factor determined by Solomon et al. (1997). Figure 26 shows the corresponding upper limit on the molecular hydrogen density of the host galaxy, and the distribution of measurements of nearby galaxies from Kennicutt (1998). The upper limits are not strongly constraining but rule out extreme gas densities in the host galaxy, a helpful starting point for learning about the nature of star formation that yields fast-ejecta SN.

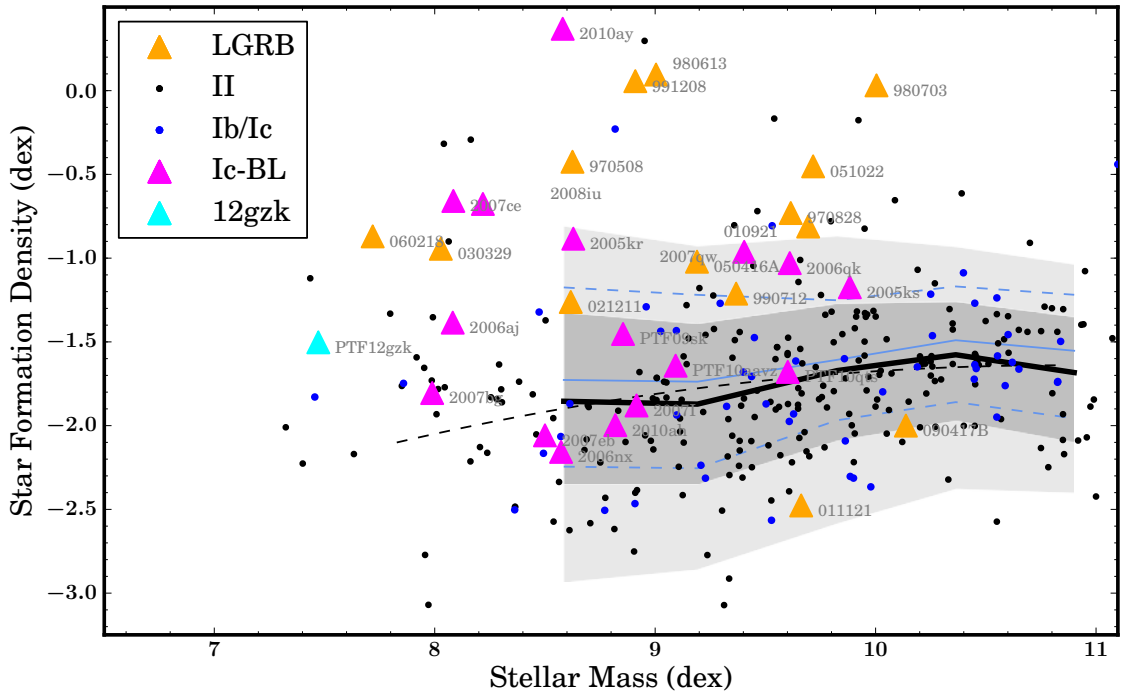


Fig. 23.— Galaxy star formation density against stellar mass. The host galaxies of $z < 0.2$ SN Ic-BL and $z < 1.2$ LGRBs show higher star formation densities than the host galaxies of Type Ib, Ic, and II core-collapse SN having typical ejecta velocities, as well as the SDSS galaxy population shown in black and blue contours. The CARMA target, the host galaxy of SN 2005ks, has a high star formation density of $10^{-1.17 \pm 0.14} M_{\odot} \text{ yr}^{-1} \text{ kpc}^{-2}$.

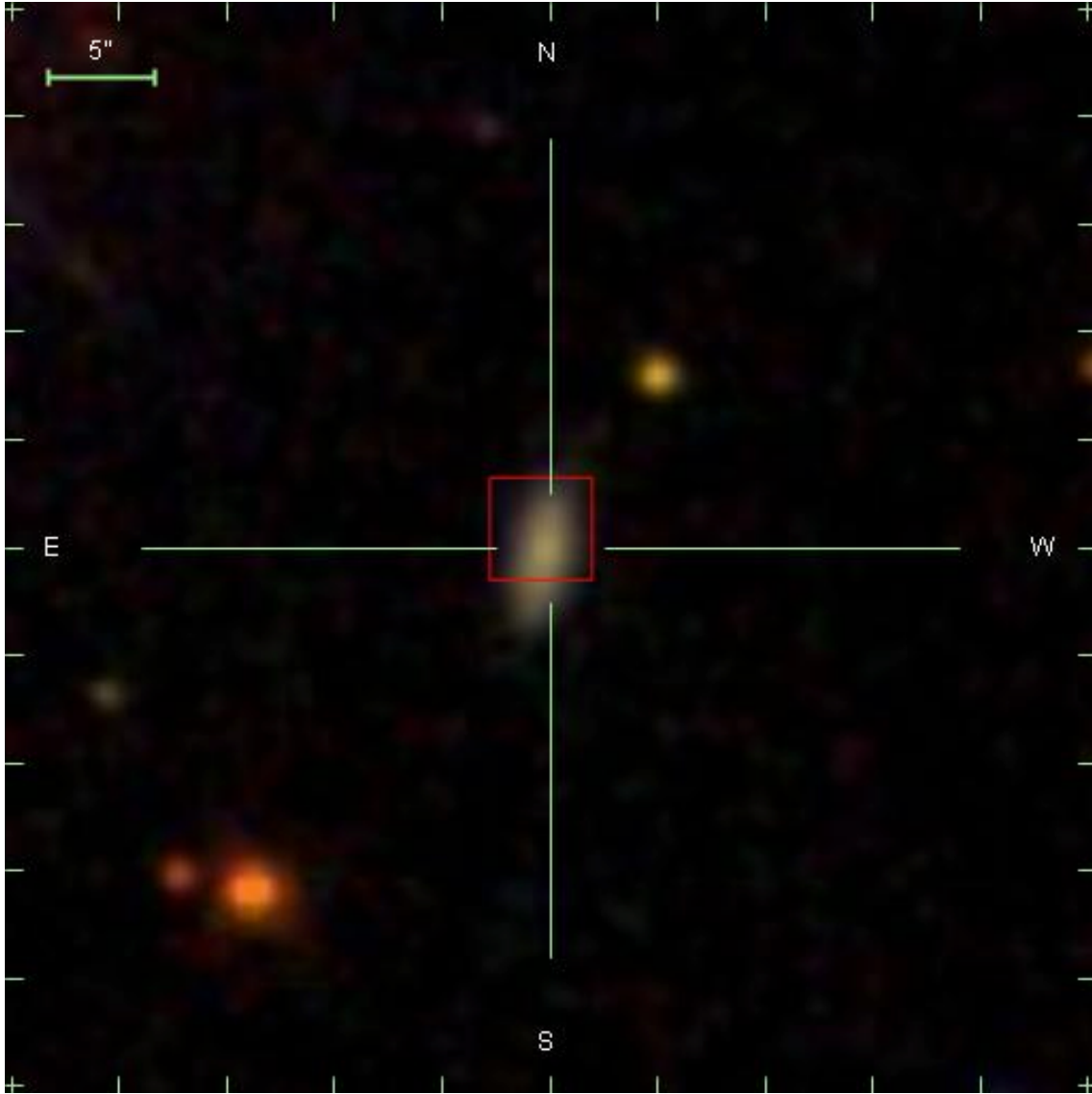


Fig. 24.— SDSS color composite image of the target $z = 0.098$ host galaxy of SN 2005kz. The red square shows the positions of the $3''$ -diameter SDSS spectroscopic fiber. The host galaxy has a semi-major axis length of $\sim 5''$.

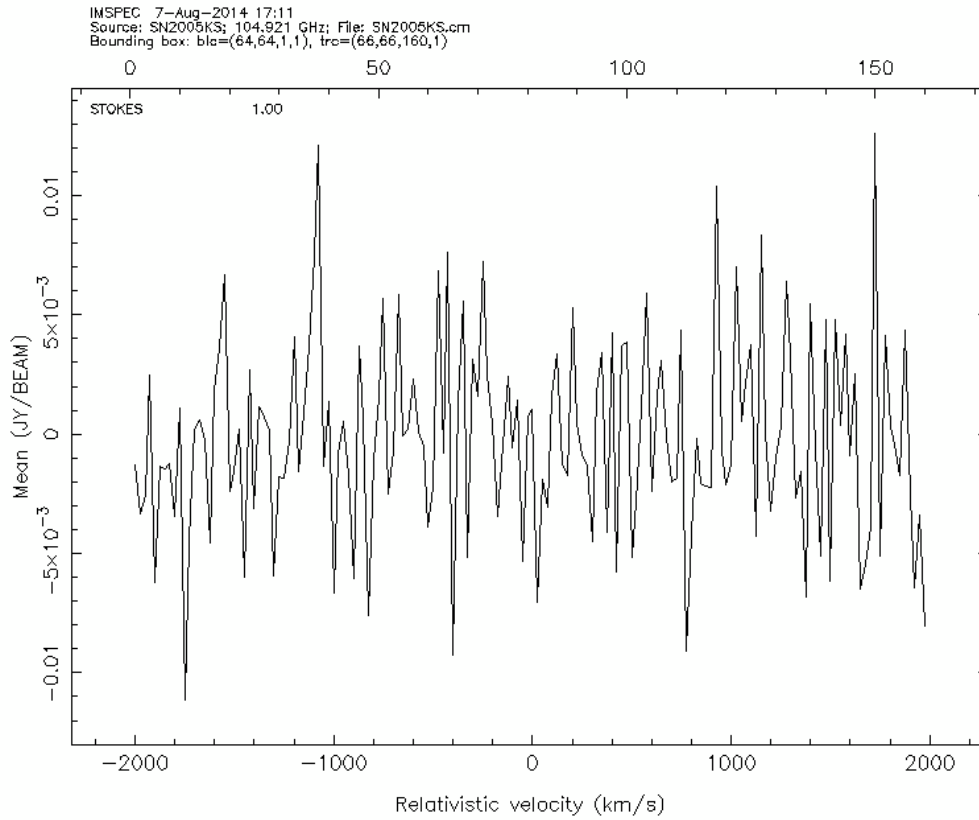


Fig. 25.— The extracted spectrum from a $5''$ square aperture positioned at field center enclosing the host galaxy optical emission. The spectrum wavelength coverage corresponds to a window that should contain $^{12}\text{CO}(1 - 0)$ emission in the host galaxy rest frame. No signal is detected, and we compute an upper flux limit that we convert to a constraint on the molecular hydrogen gas density.

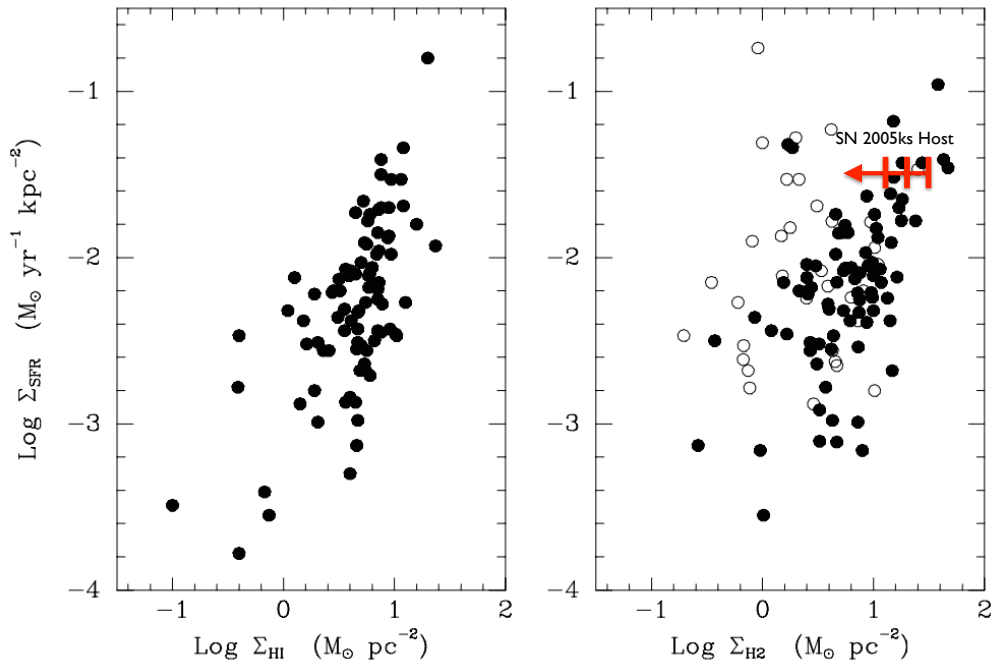


Fig. 26.— Approximate one-, two-, and three- σ limits on the molecular hydrogen density of the host galaxy of SN 2005ks from the CARMA observations superimposed on measurements of nearby galaxies from Kennicutt (1998). Filled circles show galaxies having $L_B > 10^{10} L_\odot$, while empty circles have $L_B < 10^{10} L_\odot$.

9. 1 mm Observation of M6III Red Giant Star g Her Lauren McKeown (Trinity College, Dublin)

9.1. Scientific Motivation

g Her is a semi-regular pulsating red giant star. It is particularly interesting because it has a spectral type similar to where dust first appears. All cool stars possess atmospheres heated to temperatures above that predicted by the classical assumption of Radiative Equilibrium (Schrijver & Zwaan 2000). This is due to convective motions beneath the photosphere agitating the local plasma and resulting in magnetic and acoustic disturbances, hence initiating non-radiative heating of the upper photosphere, resulting in a chromosphere. The heated plasma has a chromospheric spectrum in the UV which has been studied at length with spectrographs on IUE and HST (McMurry 1999). There exist two schools of thought on the physical structure of quiet chromospheres. The first argues that spectral signatures indicate a persistent outward temperature rise (Kalkofen et al. 1999), thought to be magnetic in origin. The second involves a time-variable plasma which is purely acoustically-shocked, where at a given position the gas temperature would fluctuate from very hot to very cool, with the mean temperature being cool (Wedemeyer-Böhm et al. 2007). This would not produce a persistent chromosphere. UV observations alone cannot determine the heating mechanism associated with these chromospheres, as persistent chromospheres and intermittently-shocked plasmas can share similar time-averaged UV emission owing to their high temperature flux sensitivity $\sim \langle e^{-\frac{h\nu}{kT}} \rangle$ when $h\nu > kT$.

Fortunately, these heated plasmas also have thermal continuum signatures at mm wavelengths (Altenhoff et al. 1994; Loukitcheva et al. 2004) where the source function is a linear function of temperature $\sim \langle T \rangle$. The intermittent and persistently formed chromosphere theories cannot satisfy both the UV and mm constraints, i.e., $\langle e^{-\frac{h\nu}{kT}} \rangle \neq e^{-\frac{h\nu}{k\langle T \rangle}}$. The mean temperature from the intermittent chromospheric model does not increase outwards like that anticipated from magnetic heating and this can be detected at mm wavelengths. Emission at a particular frequency originates from a range of atmospheric depths and hence multiple frequency observations from CARMA can infer gas temperature gradients to differentiate between the two competing models for chromospheric temperature gradients.

g Her has been observed at 1 mm by (Harper et al. 2013) using CARMA D config and by (Altenhoff et al. 1994) using the IRAM 30 m telescope. Altenhoff et al. obtained an upper limit on the flux of g Her at 250 GHz of < 6 mJy with a corresponding spectral index of < 1.0 . The red giant has also been observed by Harper et al. at 3 mm with the aim of using the flux density inferred at both wavelengths in order to determine the mm spectral index of g Her. The original observation made at 1 mm by (Harper et al. 2013) was unfortunately affected by bad weather and so follow-up continuum observations of g Her at 1 mm will allow us to determine the spectral index of g Her and hence further understand the chromospheric temperature structure of this object.

9.2. Observations and Data Reduction

g Her was observed using CARMA for over 2 hours at a rest frequency of 225 GHz. The 15-element array of 6.1 and 10.4 m antennas was in E-configuration, with baselines ranging between 8.5 m and 66 m. As this was a point-source observation, we did not mosaic our map of g Her. Mars was used as a flux calibrator, while 3C345 was observed intermittently between observing our target as a phase calibrator. 3C345 was also used as a passband calibrator. The data was calibrated using the package MIRIAD (Sault et al. 1995) Next, shadowed antennas were flagged. Data inspection indicated that antennas 7, 10, 12 and 14 required flagging for a ~ 2 min time range. Close monitoring during observations led us to source antenna collision as one of the causes for bad data during this time frame.

Our 1 mm image of g Her was produced using the MIRIAD *invert* task. To create the final map, the original map of g Her was cleaned using the *clean* task and convolved with the synthesized beam using *restor*. *Imfit* was used to fit an elliptical 2D Gaussian to our map, giving us a value for the peak flux and integrated flux from our target at 1 mm.

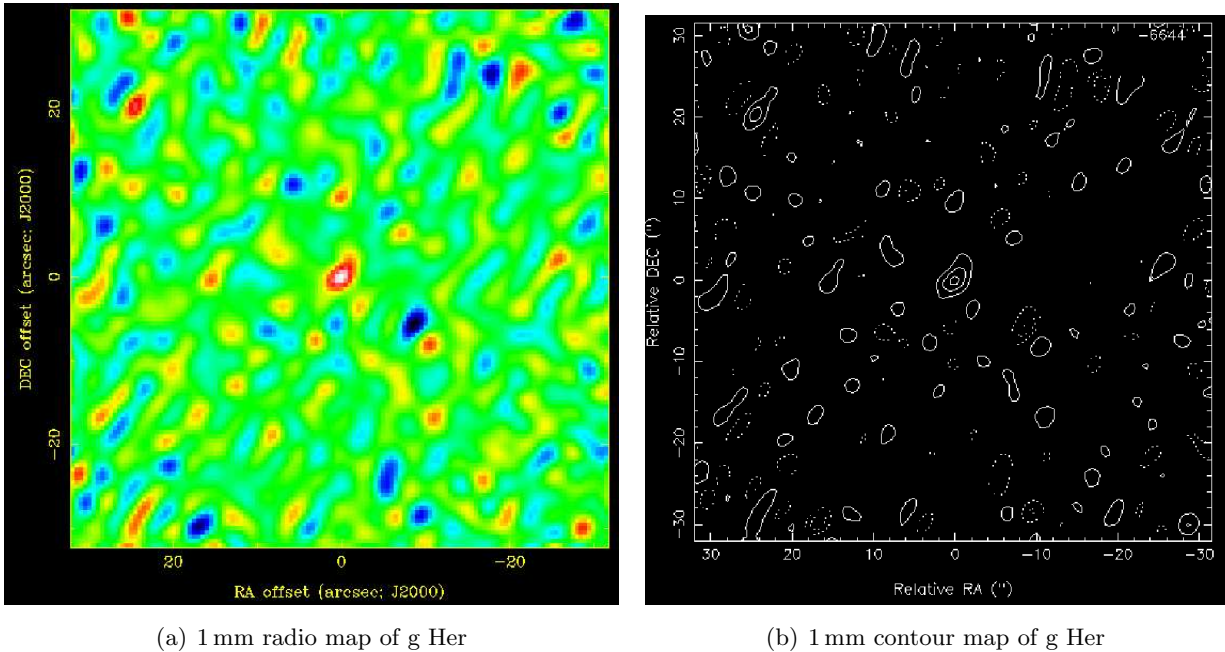


Fig. 27.— Results of CARMA 15-element array 1 mm observations of g Her

9.3. Results

The map obtained from our observations of g Her indicated a peak flux density of 21.1 ± 2.4 mJy with a noise level of 4 mJy/beam. Considering g Her is a faint source, we were still able to

identify our target at the centre of our clean map. Applying a 2D Gaussian fit to our map gave a peak flux of 18.9 ± 3.6 mJy and an integrated flux of 35 mJy. Having inspected that the box size was sufficient to surround our target and no neighboring outliers, the significant difference in peak and integrated flux density derived from applying a 2D Gaussian to our source may indicate the existence of another mm source behind our target, or contamination from background noise. The resulting peak flux of 21.1 mJy was close to the semi-analytic model prediction of (Harper et al. 2013) which was 24 mJy. We have used this flux and our CARMA 2012 observed 3mm flux to infer a preliminary spectral index for g Her of 1.62. This differs greatly from the upper limit of < 1.0 set by Altenhoff et al. (1994). An explanation for this may be that the pulsating nature of g Her may induce considerable variability at mm wavelengths and hence, comparing fluxes at 1 mm and 3 mm two years apart in calculating spectral index may not be an accurate method for the requirements of our study. We have proposed 1 mm and 3 mm follow-up observations of four red giant stars in our sample of six for CARMA semester 2014b, which includes g Her and which will allow us to further inspect whether g Her exhibits variability at these wavelengths. Combined, our CARMA observations will provide deep insight into the chromospheric thermal structure of g Her, which has not yet been explored in such detail as we propose with CARMA.

This research has been conducted with the financial support of Science Foundation Ireland under Grant Number SFI11/RFP.1/AST/3064

10. Tracing Outflows from Per-8

Erin Cox, Ko-Yun (Monica) Huang (UIUC), Dana Anderson (Caltech), & Maryam Tabeshian (Univ. of Waterloo, Ontario)

10.1. Introduction

Perseus-8, also known as IRAS 03292+3039, is a dense core in the B1 region of the Perseus molecular cloud. This molecular cloud hosts low-mass pre-main-sequence stars, embedded protostars, and starless cores within its total mass of $10,000 M_{\odot}$ and resides at a distance of 250 ± 50 pc. The classification of Per-8 has changed over time, but Schnee et al. (2012) re-classified it as a Class 0 protostar after observing its outflows in CO and $C^{18}O$. By studying the outflows of these young (having ages of a few times 10^4 years) protostars, we can learn about the structure and dynamics of their parent cloud and further our understanding of the star-formation process.

10.2. Observations

We observed the Per-8 using CARMA 3mm E-array configuration (6.1m and 10.4m antennae) on 2014 August 06. The total tracking length of time is 5.2 hours, while the actual time for our source is around 3.5 hours. The overall weather grade for our observation was given as A-.

Considering the size of the primary beam and the region of our interest, we used a 3-point mosaic to image the target region. We observed N_2H^+ (93.174Hz), HCN (88.632Hz), HCO^+ (89.189Hz), $H^{13}CO^+$ (86.754Hz), and CH_3OH (96.741Hz) with a bandwidth of 31 MHz; and three 500 MHz continuum windows were set to trace the dust mass.

3C84, one of the CARMA top tier secondary calibrators, was chosen as our phase and passband calibrator. It is a strong radio source which is 11 deg away from our source on the sky. And Uranus was adopted as our flux calibrator.

During the observation, we had been through one modification to our script for shortening the integration time for our passband calibrator 3C84. Also, at the latter phase of the observation, antenna 8 once stopped working, but resumed observing after the cycling of the power.

10.3. Data Reduction

The data were reduced using John Carpenter’s calibration and image scripts for a three-point mosaic treating the narrow and wide bands separately to detect both spectral lines and continuum emission. Data from the second integration were flagged due to the spread in passband amplitudes possibly due to a change in the passband solution after restarting the observing script. Emission from the three wide bands was combined to produce the image of the continuum emission from the source. Spectral lines were identified in channel maps of the narrowband emission averaged

over 1 km s^{-1} intervals. Using the non-spectral channels in each narrow band, the level of the continuum emission was estimated and subtracted from the total emission. Images were cleaned to a cutoff of three times the level of the root-mean-square (RMS) noise. The figures shown in the following section are the signal-to-noise maps of the combined wideband (continuum) emission and the continuum-subtracted narrowband emission from the spectral lines. Spectra were created from the narrowband emission over a 20×20 " square centered on the highest point in the dust emission observed by Schnee et al. (2012).

10.4. Results

10.4.1. Continuum

The map of the continuum emission from our source is shown in Figure 28. The point of highest emission at the center is roughly in agreement with that observed by Schnee et al. (2012). (indicated by the white star in Figure 28 and all subsequent maps).

10.4.2. N_2H^+

Figure 29 shows the outflow as seen in N_2H^+ emission. N_2H^+ is known to be a tracer of dense gas and its bulk motion. The emission maps are sampling emission from the seven hyperfine components of the $J = 1-0$ transition of N_2H^+ . Not all of the hyperfine components were resolved as seen in the spectrum provided in Figure 30.

10.4.3. HCN

HCN data is seen in Figures 31 and 32. There is evidence for an outflow seen in all three channels of the HCN maps. This is in the direction that Schnee et al. (2012) found CO to be blue shifted. The flux seen in the three separate channels is due to the three hyperfine components in the HCN line. These are also seen in the spectrum seen in Figure 32. The central velocity of these lines matches those that are found in Schnee et al. (2012).

10.4.4. HCO^+ and $H^{13}CO^+$

Maps and spectrum of HCO^+ are seen in Figures 33 and 34. There is an obvious outflow structure seen, at least in the first image (blueshifted component), and a possible redshifted component. Figures 35 and 36 show the $H^{13}CO^+$ data. The map shows that the majority of the emission is seen close to the central part of the map.

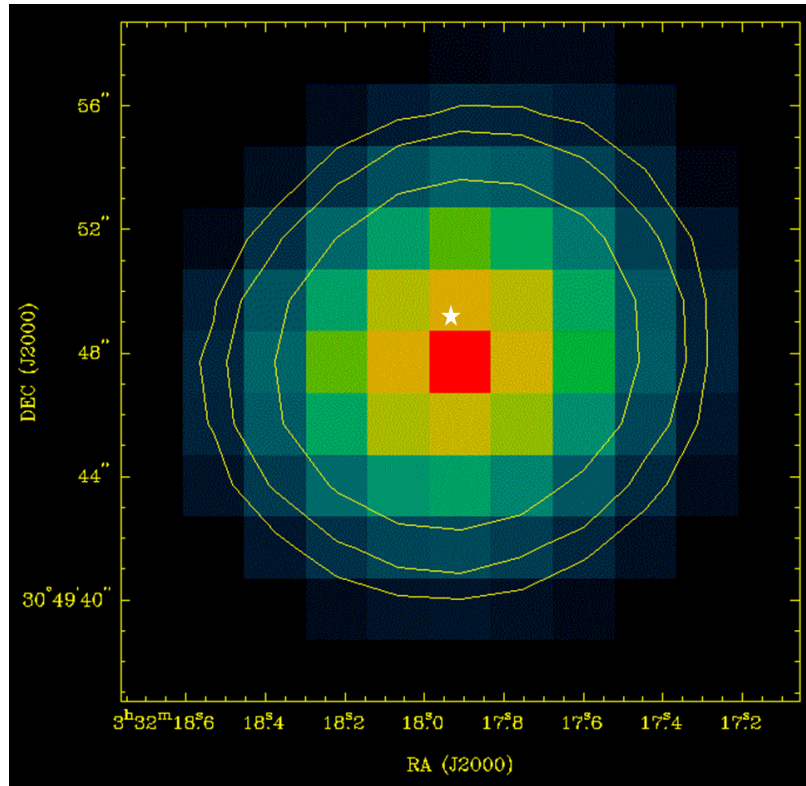
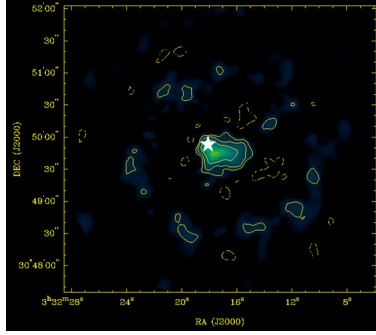
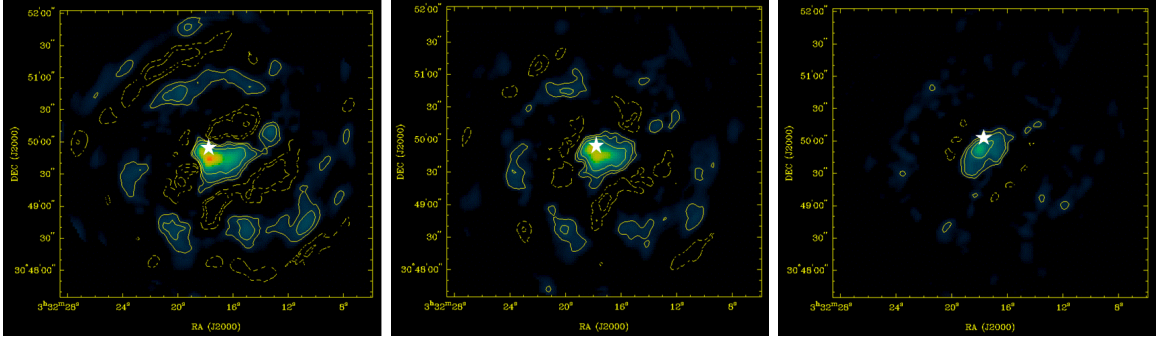


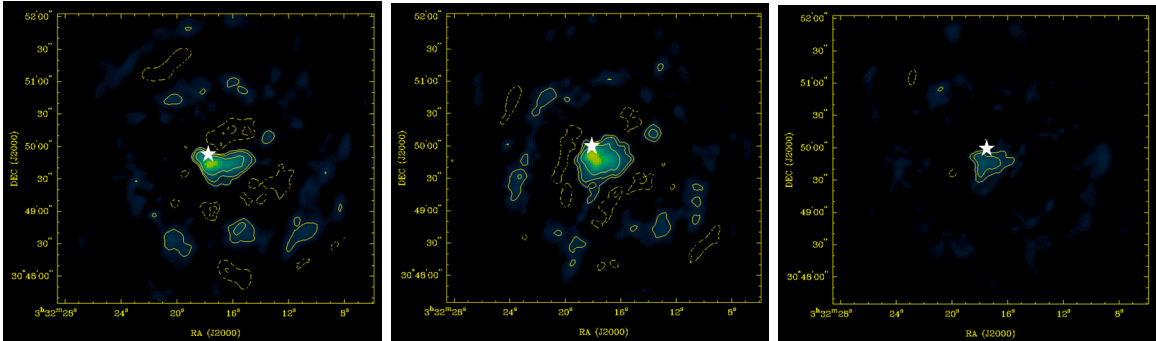
Fig. 28.— Signal-to-noise contour map of the combined wideband emission. The contour levels represent 3, 5, and 10 times the RMS noise value. The star indicates the highest point in the dust emission observed by Schnee et al. (2012). For comparison, the size of the synthesized beam is $8 \times 7''$.



(a)



(b)



(c)

Fig. 29.— Signal-to-noise contour maps of the N_2H^+ emission. The contour levels represent 3, 5, and 10 times the RMS noise value. The star indicates the highest point in the dust emission observed by Schnee et al. (2012). For comparison, the size of the synthesized beam is $8 \times 7''$. Separate components in velocity space are shown in (a), (b), and (c).

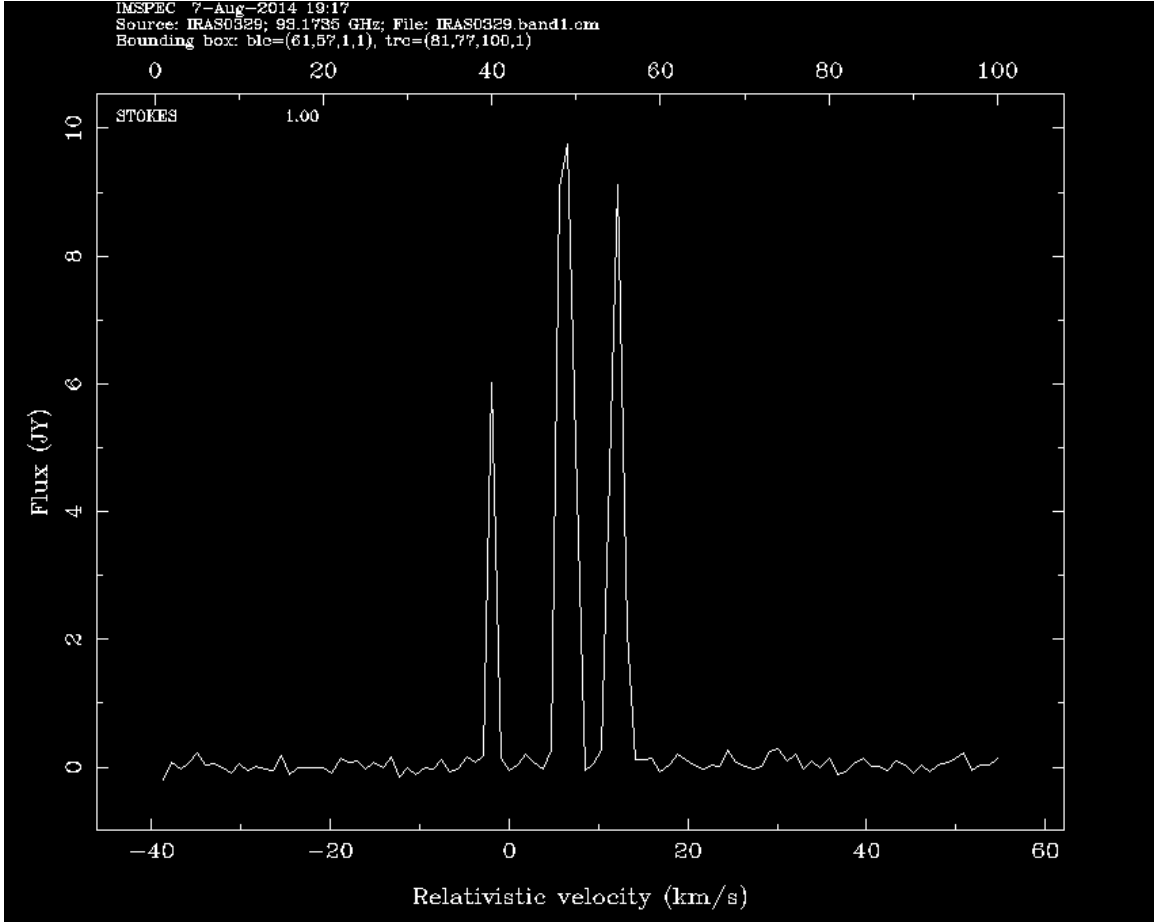


Fig. 30.— Spectrum of N_2H^+ emission

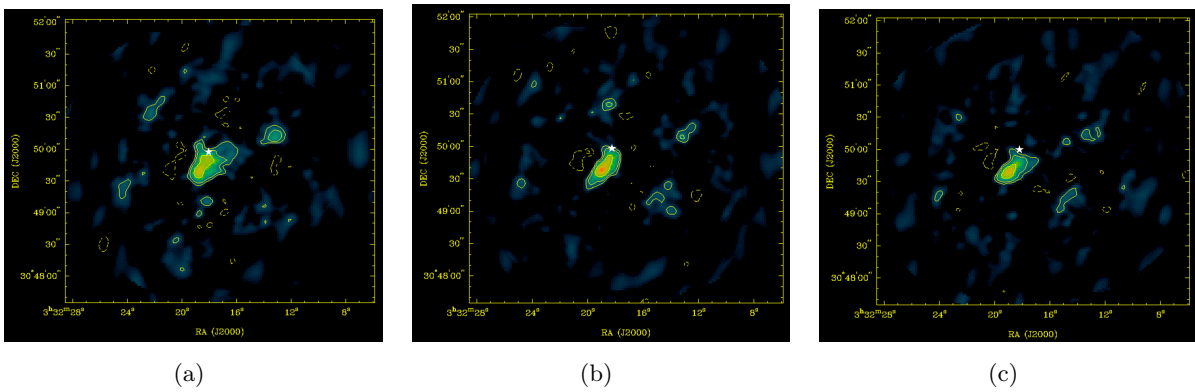


Fig. 31.— Signal-to-noise contour maps of the HCN emission. The contour levels represent 3, 5, and 10 times the RMS noise value. The star indicates the highest point in the dust emission observed by Schnee et al. (2012). For comparison, the size of the synthesized beam is $8 \times 7''$. Separate components in velocity space are shown in (a), (b), and (c).

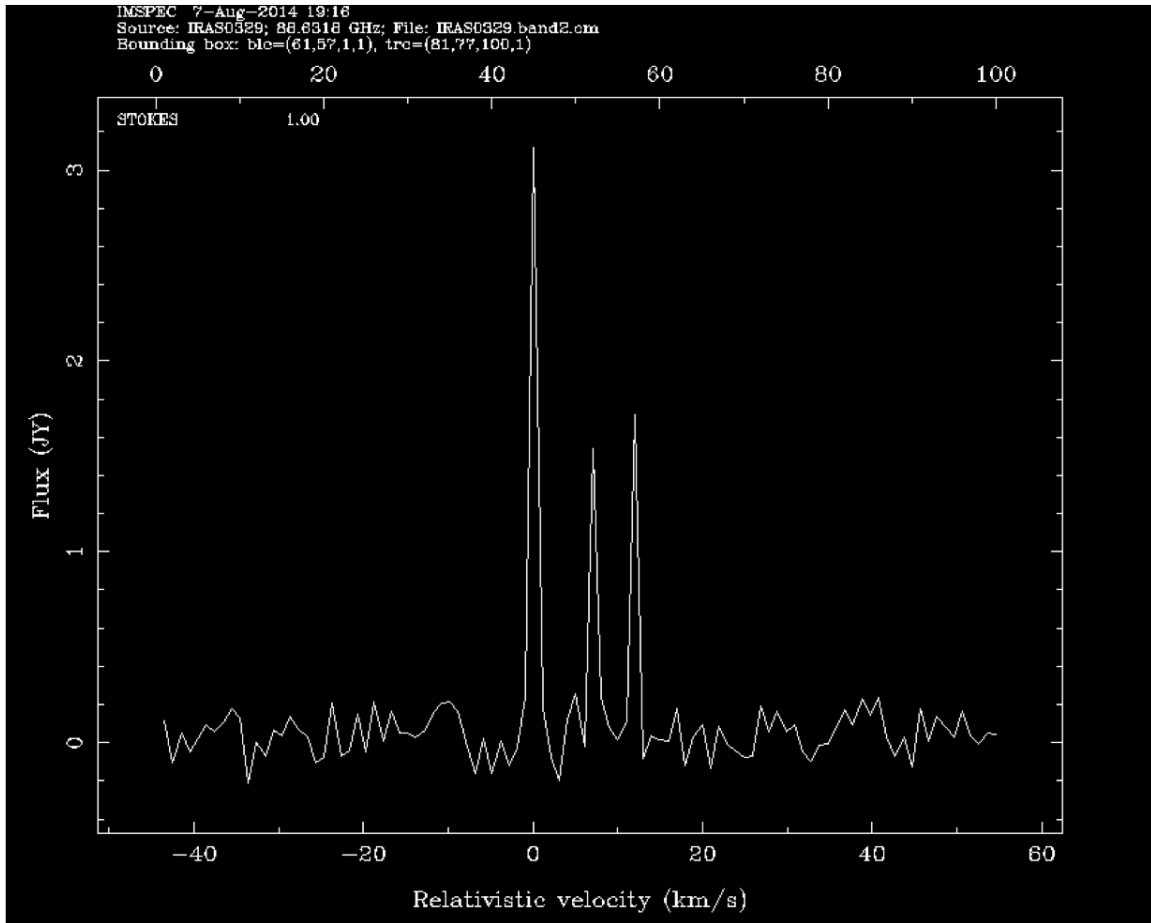


Fig. 32.— Spectrum of *HCN* emission. The three hyperfine components are resolved.

10.5. Discussion

Dust emission observed in the continuum was found to have a central point near where Schnee et al. (2012) found the point of highest dust emission. We found detections of all molecules we observed, except CH_3OH , which was not expected to be seen. The resolution of the array was not good enough to resolve all seven hyperfine components of the N_2H^+ line, but three peaks were seen, with their velocity centers consistent with what Schnee et al. (2012) measured. We were able to resolve all three of the hyperfine components in HCN , again having consistent central velocities.

We found evidence for outflows in both HCN and HCO^+ . Both maps have a blue shifted component of an outflow, and the HCO^+ maps show signs for a possible redshifted component as well. Though, given the level of contours seen, we cannot say if there definitely is. In N_2H^+ and in $H^{13}CO^+$ we see the largest flux near the center of the field, close to where the largest dust emission is coming from. While all of these molecules trace bulk motion, N_2H^+ tracks the densest material, so it makes sense that outflows are not seen using it. The definite outflow structure seen in HCO^+ is an exciting result. This is because, while it's predicted to be a large part of protostars, it has not been detected very many times.

We hope to analyze this data using different techniques, such as moment maps or PV diagrams, to get a better constraint of where the gas really is. This can help narrow down what processes are really happening, and where. For future work, it would be ideal to also observe CO isotopes and the polarization of the dust grains. This will again give a broader view of what is actually happening in near the protostar.

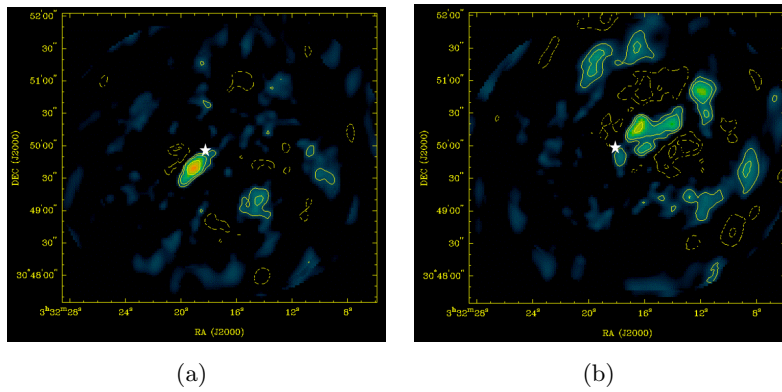


Fig. 33.— Signal-to-noise contour maps of the HCO^+ emission. The contour levels represent 3, 5, and 10 times the RMS noise value. The star indicates the highest point in the dust emission observed by Schnee et al. (2012). For comparison, the size of the synthesized beam is $8 \times 7''$. These are not separate velocity components, the different maps are a consequence for how the channels were binned.

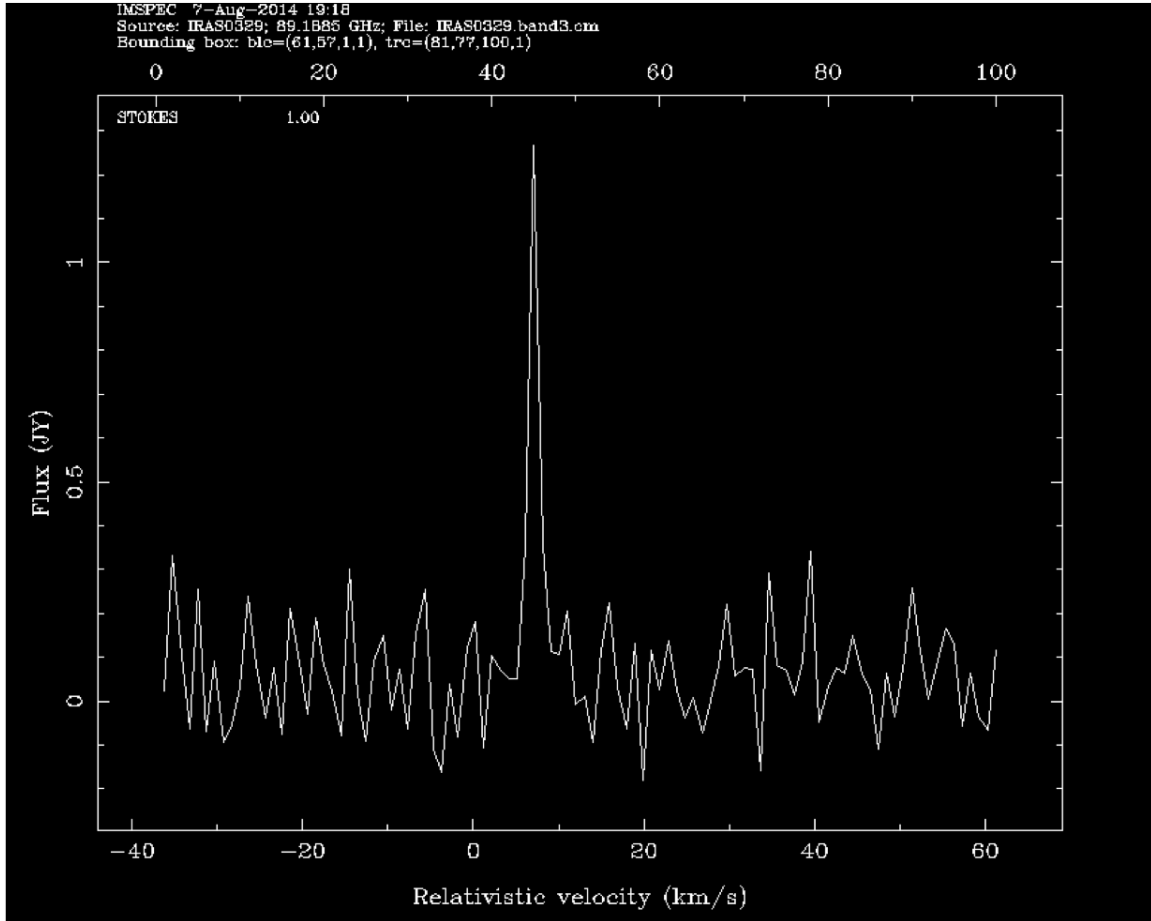
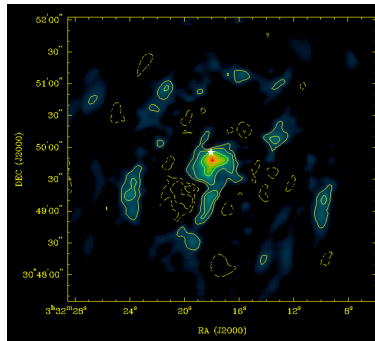


Fig. 34.— Spectrum of HCO^+ emission.



(a)

Fig. 35.— Signal-to-noise contour maps of the $H^{13}CO^+$ emission. The contour levels represent 3, 5, and 10 times the RMS noise value. The star indicates the highest point in the dust emission observed by Schnee et al. (2012). For comparison, the size of the synthesized beam is $8 \times 7''$.

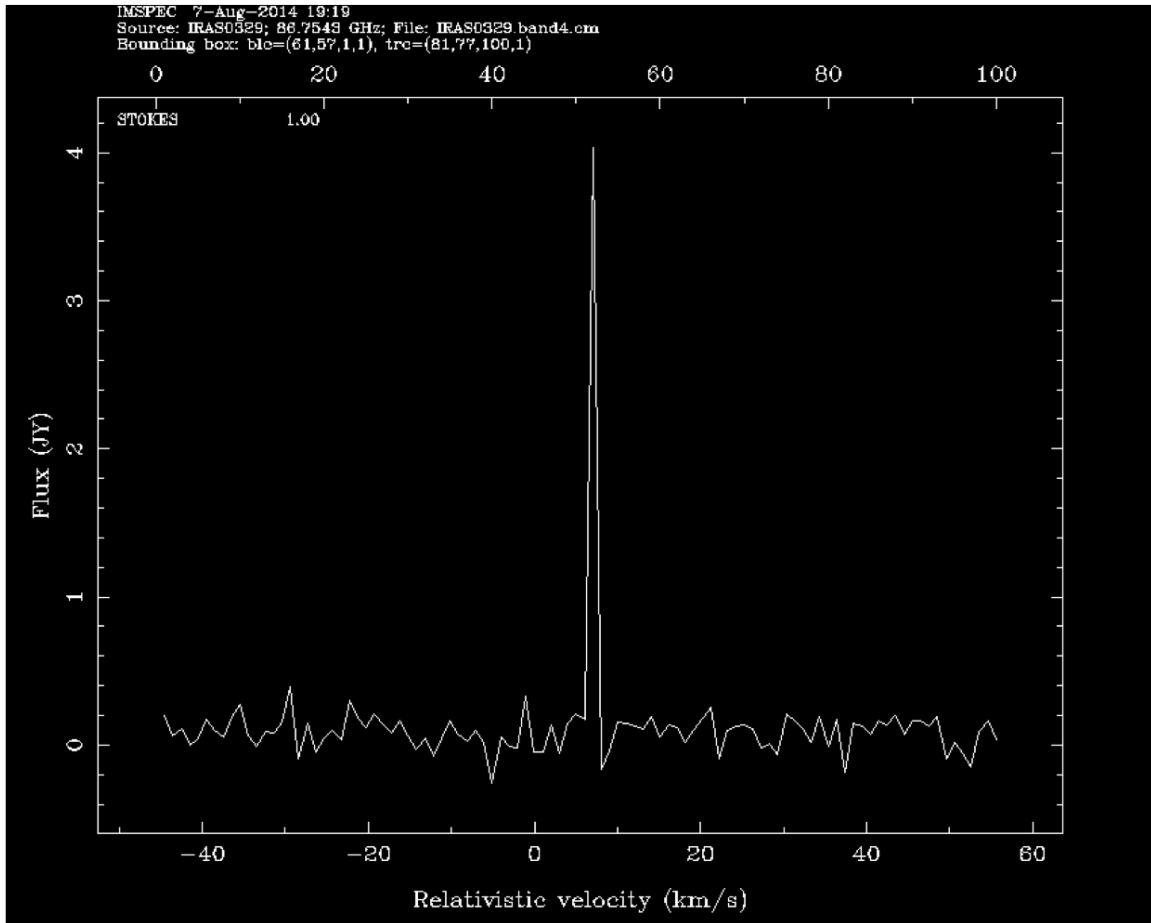


Fig. 36.— Spectrum of $H^{13}CO^+$ emission.

11. Observing a massive galaxy cluster at medium redshift

Jay Franck (Case Western Reserve), Andrew Nadolski (UIUC), Bandon Decker
(Univ. Missouri, Kansas City)

11.1. Background

Galaxy clusters are the largest gravitationally bound objects in the universe; as such, they make excellent cosmological probes. The majority of the baryonic mass of a galaxy cluster is in the form of an electron plasma known as the intracluster medium (ICM). This gas emits thermally in the X-ray, but it also inversely Compton scatters the cosmic microwave background radiation (CMB) Sunyaev & Zeldovich (1975). For the frequencies at which we looked, this effect manifests as a decrement appears in the otherwise uniform CMB. This is the Sunyaev-Zel'Dovich effect; the magnitude of the decrement is related to the density of the ICM along the line of sight which is in turn related to the mass of the cluster Andersson et al. (2011). The SZ effect is largely independent of redshift, making it an excellent tool for measuring the mass of distant galaxy clusters.

11.2. Observation

To fulfill the goals outlined for CARMA Summer School 2014, it was of paramount importance to observe an object that is known to have an easily identifiable signal. For this reason, we chose MACSJ0717.5+3745 as it is an incredibly massive cluster with an estimated mass of $M(r < 1\text{Mpc}) > 2 \times 10^{15} M_{\odot}$ at a redshift of $z = 0.55$ Limousin et al. (2012). When considering potential weather issues, the need for a structure that could be detected by the SZ effect in a minimum amount of time was important. Clusters in the high redshift regime (especially at $z \geq 1$ require larger time commitments Muchovej et al. (2007); Culverhouse et al. (2010), even upwards of 50 hours of on source time Mantz et al. (2014).

We began observations on August 5, 2014 at 04:43 LST. Our track time totaled 5.2 hours, 3.8 of which were spent on source. The remaining time was devoted to phase calibration using J0646+448. We were unable to observe a flux calibrator. We conducted observations at 30Ghz using the SZA antennae. Weather conditions were generally poor. Sky RMS was consistently 1000 microns or greater and τ_{230} ranged from 0.57 to 2.71. Consequently, a great deal of data flagging (including cuts to time, system temperature, and baselines) was required to produce a clean map.

11.3. Results

With a track length of only ~ 5 hours, of which 3.4 hours was on source, we were able to detect an SZ decrement from MACSJ0717.5+3745 (pointed at RA 07:17:31.7 and DEC +37:45:18.2) at a significance level of $> 8\sigma$ from the RMS noise. Figure 37 shows the clean map of the cluster's SZ effect. Based on the relatively small track time used, these authors recommend this cluster for the

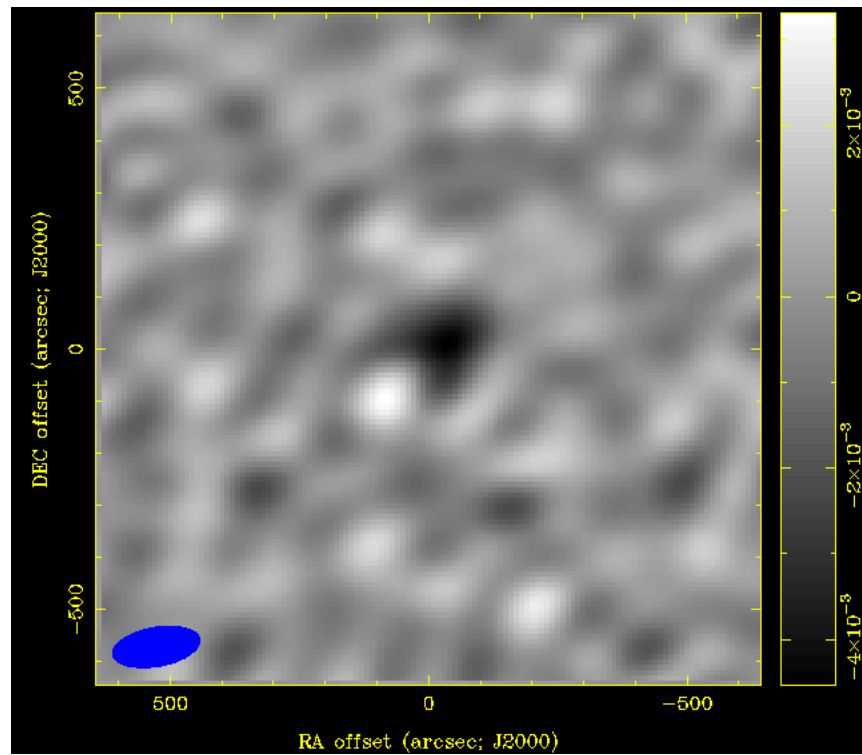


Fig. 37.— The Sunyaev-Zel’Dovich decrement observed for MACSJ0717.5+3745 at 30 GHz at a significance level of $> 8\sigma$.

target of future CARMA Summer School projects.

12. Observations of ^{12}CO and ^{13}CO in Molecular Outflow L1228 A

Amy Steele (University of Maryland) and Ned Molter (Macalester College)

12.1. Introduction

Molecular outflows are a type of mass-loss phenomena associated with the earliest stages of stellar evolution. Emission maps of molecular flows reveal cloud structure and provide insight on the initial conditions of the star formation process. Additionally, the flows constrain models of cloud collapse and star formation, since the flow momentum leaves a fossil record of the mass loss history of the centrally embedded protostar (Bally et al. 1995).

We observed a warm, compact source as well as ^{12}CO and ^{13}CO in the molecular outflow of the L1228 cloud. L1228 is located at ~ 200 pc and is part of the Cepheus flare, a giant molecular cloud complex in Cepheus, which is also part of the Gould’s Belt system (Bally et al. 1995). The cloud spans 0.086 square degrees and has a $v_{\text{LSR}} = -7.6$ km/s (Bally et al. 1995). L1228 consists of three centers of star formation (Kun et al. 2008), one of those being the L1228 core, or L1228 A. We focus on L1228 A in this memo (α : 20:57:13, δ : 77:35:44), as it contains the Class I source IRAS 20582+7724, which is driving the outflow.

Millimeter wavelength observations of the region reveal continuum emission from warm dust surrounding the young star as well as red- and blueshifted bipolar outflows showing bulk motions.

12.2. Observations

We observed L1228 for 3.1 hours on August 6, 2014 using the CARMA-15 array in its compact E configuration with baselines ranging from 8.5 m to 66 m. The flux was calibrated at the beginning of the track using Neptune. Quasar 3C454.3 was also observed once at the beginning of the track to calibrate the bandpass by measuring channel-to-channel variations of the correlator. Observations of the point-like source 1927+739 were interleaved with the science target to follow the behavior of the atmosphere and instrumental phase during the track. The overall grade for the track was a ‘B’ since the sky phase RMS was $\sim 346 \mu\text{m}$, and τ hovered around 1.8. The correlator was setup such that the LO frequency was 108 GHz with the continuum source observed in five 500 MHz windows in the upper and lower sidebands. The lower sideband was also configured to potentially observe C^{18}O , ^{13}CO , and ^{12}CO in narrowband 31 MHz windows. Additionally, we only observed LL polarization, even though CARMA is capable of observing 4: LL, RR, LR, RL.

12.3. Data Reduction

The resulting data was calibrated using MIRIAD software³, and initially inspected using John Carpenter’s data reduction script. After inspecting the data, we found that no flagging was necessary. We then wrote a script that would calibrate the data from this specific observation. The passband, flux, and gain were calibrated using the `mfcal`, `bootflux`, and `mselfcal` routines. After calculating the gain, it was applied to the narrowband CO data. The routine `mselfcal` was run on the phase calibrator to find the offset between the narrow- and widebands. After calibration, we took the Fourier transform of the sky distribution (`invert`), ran a CLEAN algorithm (`clean`), and then re-convolved the cleaned components with the beam (`restor`). Maps of the distribution of CO and the continuum source are provided in figures 1-4.

12.4. Results

We detected ^{12}CO , ^{13}CO , and a continuum source (see figure 40) toward L1228. The CO emission is overall spatially aligned with the compact continuum source. Based on line velocity maps of the CO isotopes, we did not detect ^{18}CO . Integrated intensity maps of the zeroth moment show that the ^{12}CO is extended in the east-west direction (see figure 38). The emission in the east direction is blueshifted, while the emission in the west direction is redshifted. The maps of the ^{13}CO also show some bulk motion (see figure 39), though not as spatially extended as the ^{12}CO . The radial velocity of the source is reflected in the central line velocity of the CO emission lines (see figure 42). The ^{12}CO shows a double-peaked velocity structure indicative of bulk motion from the outflow centered at the LSR velocity of L1228 A (-7.6 km/s). However, the ^{13}CO shows a single peak centered near the system velocity, suggesting that this emission originates from a region close to the embedded source. These results are consistent with the ^{12}CO and ^{13}CO maps from Bally et al. 1995. A full image of the region is shown in figure 41.

³See <http://www.cfa.harvard.edu/sma/miriad/>.

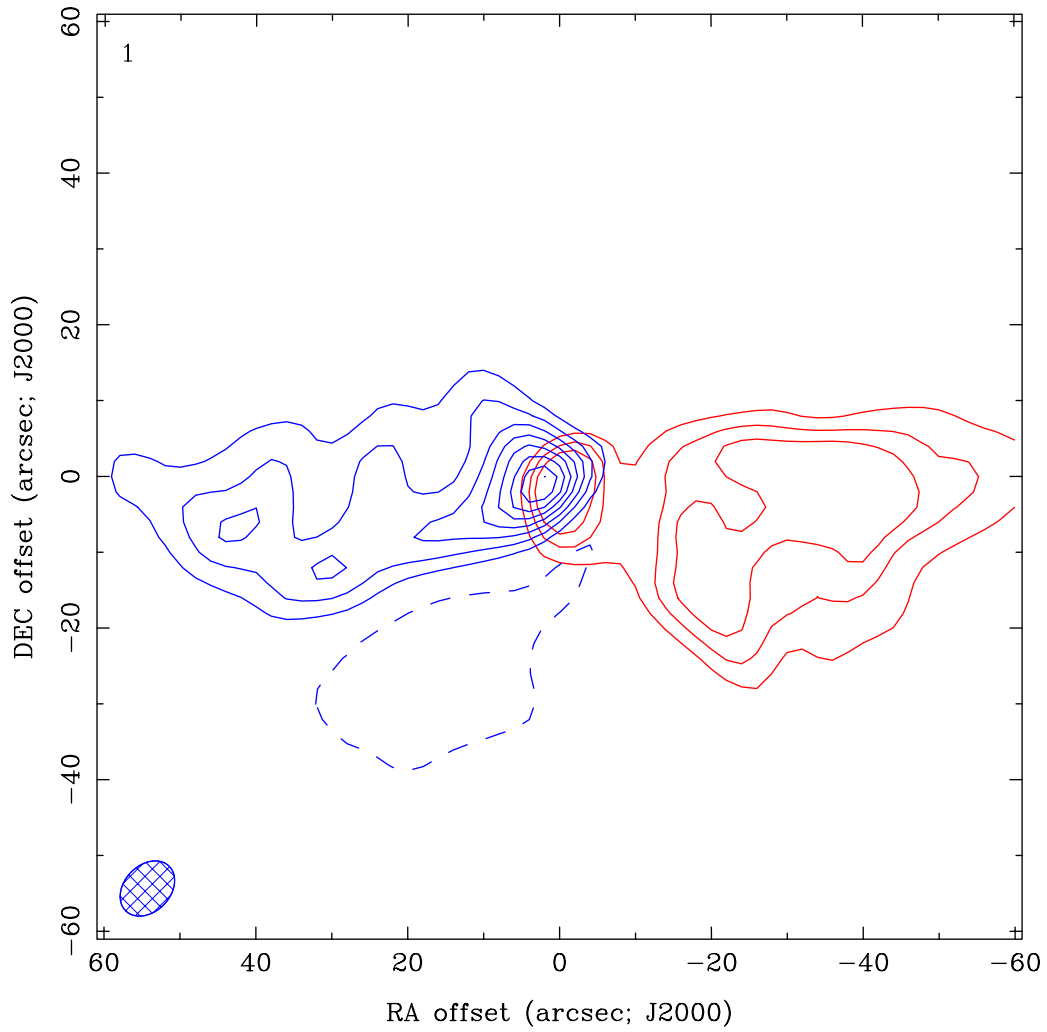


Fig. 38.— Molecular outflow L1228 A. A map of ^{12}CO with red contours at $3, 6,$ and $9 \times \text{RMS}$. Blueshifted emission is shown in solid blue, and redshifted emission is shown in red. Dashed lines show negative contours. The size is the synthesized beam is shown with the blue hatched oval.

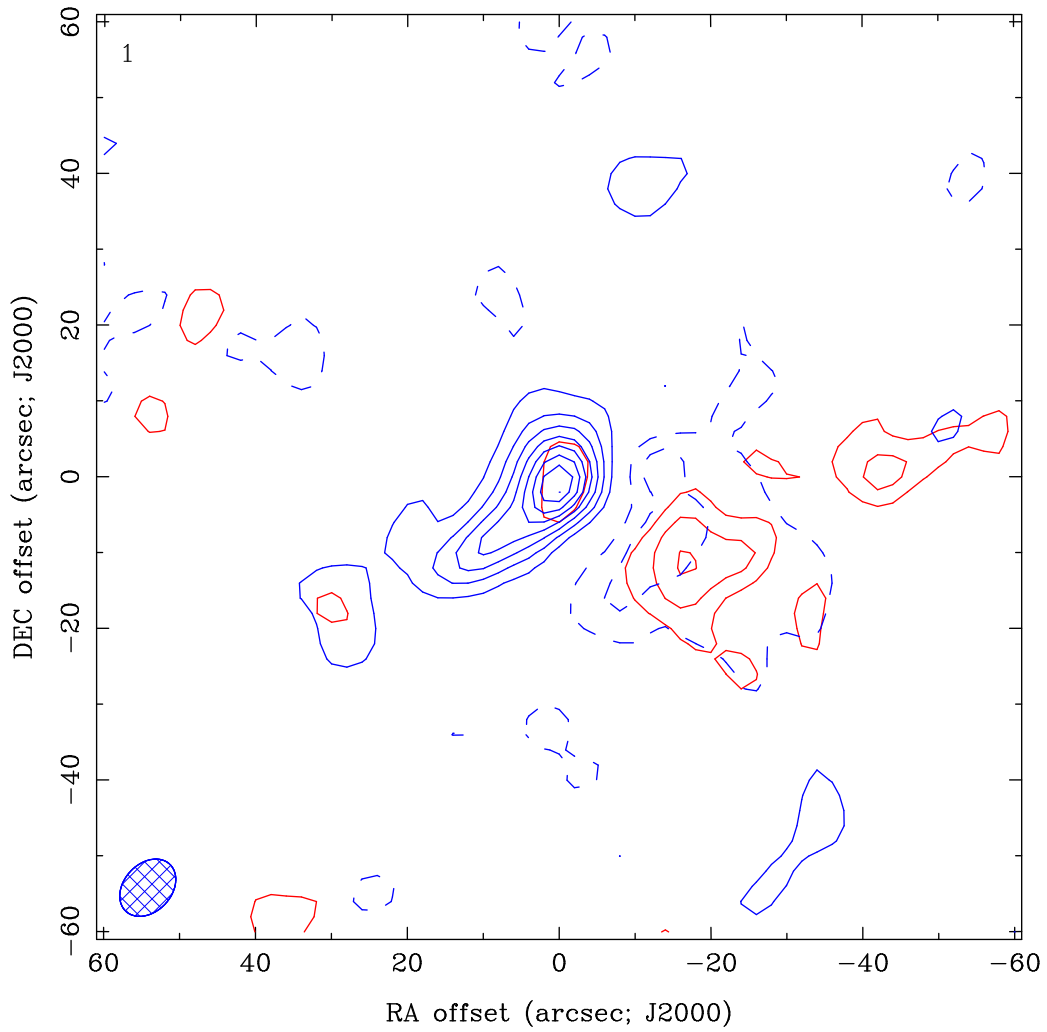


Fig. 39.— Molecular outflow L1228 A. A map of ^{13}CO with red contours at $3, 6,$ and $9 \times \text{RMS}$. Blueshifted emission is shown in solid blue, and redshifted emission is shown in red. Dashed lines show negative contours. The size the synthesized beam is shown with the blue hatched oval.

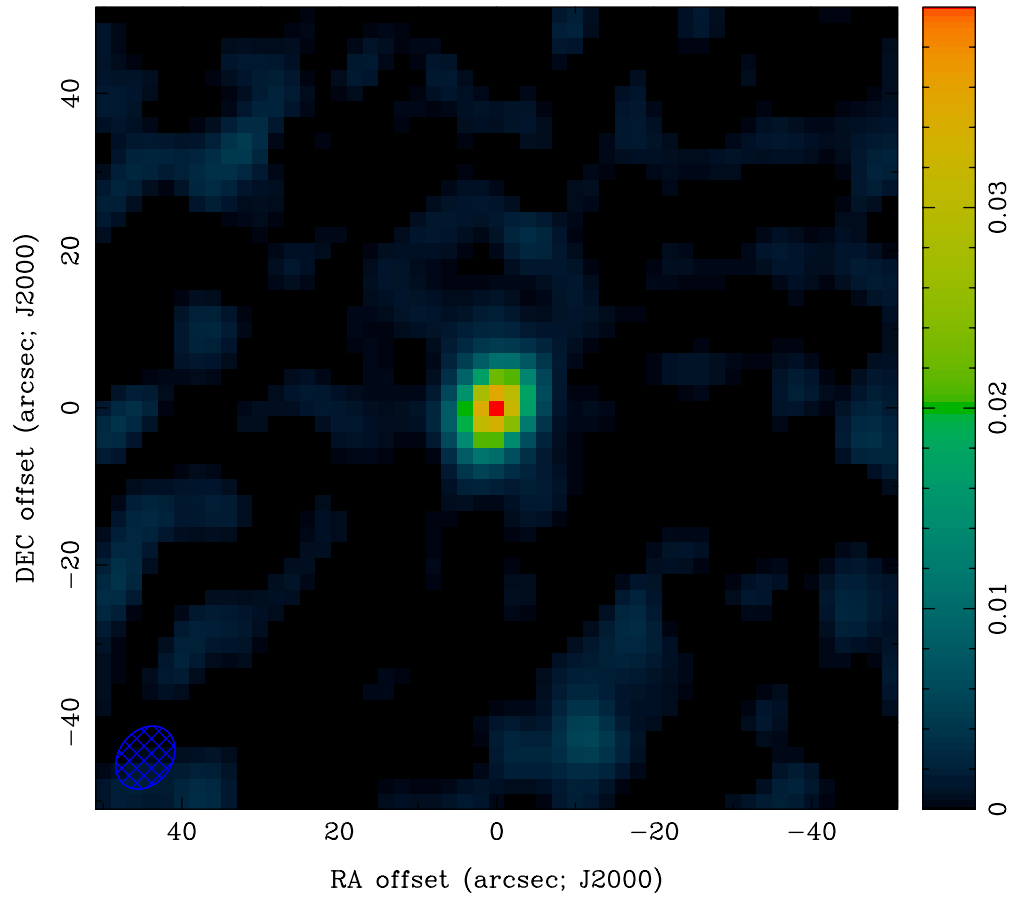


Fig. 40.— Molecular outflow L1228 A. A map of the continuum at 0.3 cm with 0.04 Jy/beam.

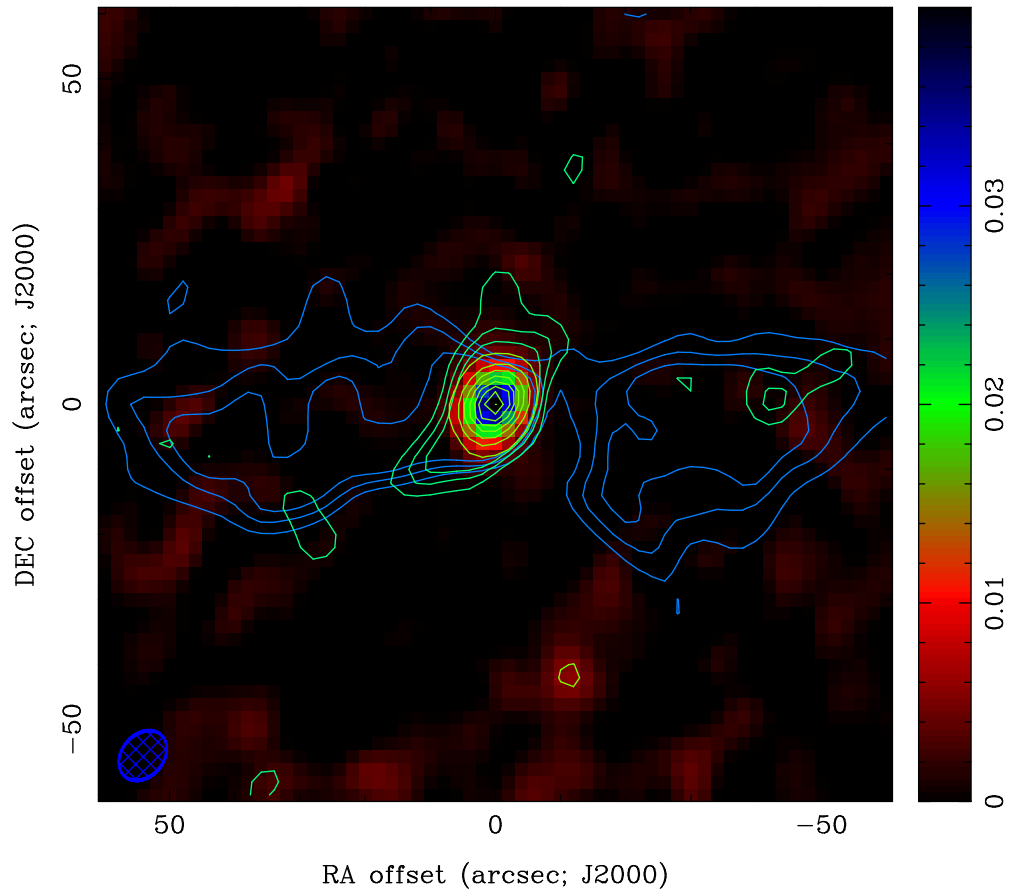


Fig. 41.— Molecular outflow L1228 A. A map of ^{12}CO (in blue), ^{13}CO (in green), and 0.28 mm continuum (pixelated at the center). The contours for the ^{12}CO and ^{13}CO are at $3, 6,$ and $9 \times \text{RMS}$.

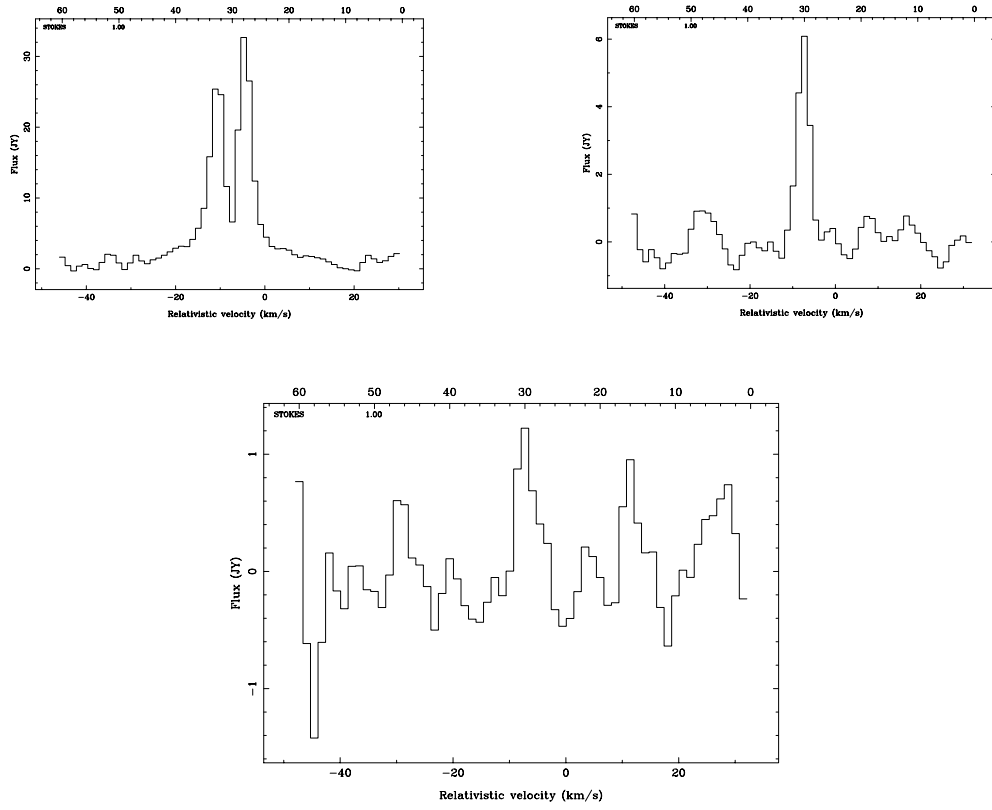


Fig. 42.— Spectra of the CO in the direction of L1228 A. Top: left, ^{12}CO ; right, ^{13}CO . Bottom: the non-detection of ^{18}CO .

E-mail addresses

Patrick Kelly (UCB), patrick.l.kelly@gmail.com
Lauranne Lanz (CIT), llanz@ipac.caltech.edu
Lauren McKeown (TCD), mckeowla@tcd.ie
Scott Barenfeld (CIT), scott.barenfeld@gmail.com
Devin Crichton (JHU), dcrichto@pha.jhu.edu
Jonathan Florez (Fisk), jflorez0206@gmail.com
Amy Steele (Wesleyan), amysteale08@gmail.com
Ned Molter (Macalester), emolter@macalester.edu
Joey Rodriguez (Vanderbilt), rodriguez.jr.joey@gmail.com
Bandon Decker (UMKC), bbdz86@mail.umkc.edu
Jay Franck (CWRU), jrf110@case.edu
Shravan Avadhuta (CSU-LA), savadhu@calstatela.edu
Maryam Tabeshian (UWO), mtabeshi@uwo.ca
Dana Anderson (CIT), deanders@caltech.edu
Ko-Yun Huang (UIUC), khuang33@illinois.edu
Erin Cox (UIUC), egcox2@illinois.edu

REFERENCES

- Alatalo, K., et al. 2013, MNRAS, 432, 1796
- Altenhoff, W. J., Thum, C., & Wendker, H. J. 1994, A&A, 281, 161
- Andersson, K., et al. 2011, ApJ, 738, 48
- Bally, J., Devine, D., Fesen, R. A., & Lane, A. P. 1995, ApJ, 454, 345
- Beasley, A. J., Gordon, D., Peck, A. B., Petrov, L., MacMillan, D. S., Fomalont, E. B., & Ma, C. 2002, ApJS, 141, 13
- Bigiel, F., Leroy, A., Walter, F., Brinks, E., de Blok, W. J. G., Madore, B., & Thornley, M. D. 2008, AJ, 136, 2846
- Cabrit, S., Pety, J., Pesenti, N., & Dougados, C. 2006, A&A, 452, 897
- Cappellari, M., et al. 2011, MNRAS, 413, 813
- Carlstrom, J. E., Holder, G. P., & Reese, E. D. 2002, arXiv preprint astro-ph/0208192
- Coble, K., et al. 2007, AJ, 134, 897
- Condon, J. J., Cotton, W. D., Greisen, E. W., Yin, Q. F., Perley, R. A., Taylor, G. B., & Broderick, J. J. 1998, AJ, 115, 1693

- Culverhouse, T. L., et al. 2010, *ApJ*, 723, L78
- De Lucia, G., Kauffmann, G., & White, S. D. 2004, *Monthly Notices of the Royal Astronomical Society*, 349, 1101
- Fruscione, A., et al. 2006, in *Society of Photo-Optical Instrumentation Engineers (SPIE) Conference Series*, Vol. 6270, *Society of Photo-Optical Instrumentation Engineers (SPIE) Conference Series*
- Guillard, P., et al. 2012, *ApJ*, 747, 95
- Harper, G. M., O’Riain, N., & Ayres, T. R. 2013, *MNRAS*, 428, 2064
- Hasselfield, M., et al. 2013, *J. Cosmology Astropart. Phys.*, 7, 8
- Kalkofen, W., Ulmschneider, P., & Avrett, E. H. 1999, *ApJ*, 521, L141
- Kelly, P. L., Filippenko, A. V., Modjaz, M., & Kocevski, D. 2014, *ApJ*, 789, 23
- Kennicutt, Jr., R. C. 1998, *ApJ*, 498, 541
- Kun, M., Kiss, Z. T., & Balog, Z. 2008, *Star Forming Regions in Cepheus*, 136
- Leroy, A., Bolatto, A. D., Simon, J. D., & Blitz, L. 2005, *ApJ*, 625, 763
- Leroy, A. K., et al. 2009, *AJ*, 137, 4670
- Limousin, M., et al. 2012, *A&A*, 544, A71
- Loukitcheva, M., Solanki, S. K., Carlsson, M., & Stein, R. F. 2004, *A&A*, 419, 747
- Mantz, A. B., et al. 2014, *ArXiv e-prints*
- McMurry, A. D. 1999, *MNRAS*, 302, 37
- Melbourne, J., et al. 2012, *ApJ*, 748, 47
- Miller, B. W., & Hodge, P. 1996, *ApJ*, 458, 467
- Motl, P. M., Hallman, E. J., Burns, J. O., & Norman, M. L. 2005, *ApJ*, 623, L63
- Muchovej, S., et al. 2007, *ApJ*, 663, 708
- Mushotzky, R., & Loewenstein, M. 1997, *The Astrophysical Journal Letters*, 481, L63
- Ogle, P., Boulanger, F., Guillard, P., Evans, D. A., Antonucci, R., Appleton, P. N., Nesvadba, N., & Leipski, C. 2010, *ApJ*, 724, 1193
- Osterloh, M., & Beckwith, S. V. W. 1995, *ApJ*, 439, 288

- Rodriguez, J. E., Pepper, J., Stassun, K. G., Siverd, R. J., Cargile, P., Beatty, T. G., & Gaudi, B. S. 2013, *AJ*, 146, 112
- Roussel, H. 2013, *PASP*, 125, 1126
- Sault, R. J., Teuben, P. J., & Wright, M. C. H. 1995, in *Astronomical Society of the Pacific Conference Series*, Vol. 77, *Astronomical Data Analysis Software and Systems IV*, ed. R. A. Shaw, H. E. Payne, & J. J. E. Hayes, 433
- Schmidt, M. 1959, *ApJ*, 129, 243
- Schnee, S., Sadavoy, S., Di Francesco, J., Johnstone, D., & Wei, L. 2012, *ApJ*, 755, 178
- Schrijver, C. J., & Zwaan, C. 2000, *Irish Astronomical Journal*, 27, 65
- Solomon, P. M., Downes, D., Radford, S. J. E., & Barrett, J. W. 1997, *ApJ*, 478, 144
- Stephens, I. W., et al. 2013, *ApJ*, 769, L15
- Sunyaev, R. A., & Zeldovich, I. B. 1975, *MNRAS*, 171, 375
- . 1980, *ARA&A*, 18, 537
- Taylor, G. 1997, *The Difmap Cookbook*
- Walter, F., & Brinks, E. 1999, *AJ*, 118, 273
- Wang, Z., Kenney, J. D. P., & Ishizuki, S. 1992, *AJ*, 104, 2097
- Wedemeyer-Böhm, S., Ludwig, H. G., Steffen, M., Leenaarts, J., & Freytag, B. 2007, *A&A*, 471, 977
- Weisz, D. R., Skillman, E. D., Cannon, J. M., Walter, F., Brinks, E., Ott, J., & Dolphin, A. E. 2009, *ApJ*, 691, L59
- Zhang, T.-J., & Wu, X.-P. 2000, *The Astrophysical Journal*, 545, 141